October 2017

Master Thesis Draft

Frederik S. Møller
IFA, Aarhus University

Contents

1 Introduction

Ultracold atoms present an extremely powerful tool in quantum reasearch. At the scale of nanokelvins thermal effects no longer destroy the otherwise fragile quantum systems. Thus, quantum phenomena, otherwise only known from theory, can be studied directly. Atomic physics experiments with such ultracold, quantum degenerate gases offer some unique features: (i) a wide range of Hamiltonians can be mapped to the systems making experiments highly customizable. This can in part be attributed to (ii) the very high degree of control achievable through the manipulation of external fields. Through this, the cold atoms can be trapped and manipulated using magnetic and optical traps. Furthermore, the collisional properties of the atoms can be tuned through magnetic Feshbach resonances, and the properties of the gas can be probed through interactions between internal energy levels of the atoms and laser light [16, 2].

In the regime of such cold temperatures many-body phenomena such as Bose-Einstein condensation takes place, where the ground state of a system gains a macroscopic populations. Ever since the first realisation of a Bose-Einstein condensate in 1995 [1], the special properties of this macroscopic quantum state have been used in a wide range of experiments. One method of utilizing Bose-Einstein condensates is to load them into an optical lattice, which is an array of potentials created through the atoms dipole interaction with laser beams. By utilizing the high controllability of these systems, one can perform quantum simulations of various systems, such as spin chains [34], Dirac cones [37], and artificial gauge fields [6]. Furtermore, the properties of cold atoms in optical lattices is very favourable for experiments in quantum information, where quantum gates can be realised through controlled collisions [14] or Rydberg atoms [31].

This note presents the basic theory of quantum many-body systems in optical lattices.

2 Optical Lattice Potentials

Cold atoms can be trapped in potentials generated by their own dipole interaction with light. Thus, superimposing laser beams allows one to create optical lattices in various shapes and forms. Such dipole traps realised using far-detuned light have important properties, as (i) they are capable of trapping neutral atoms, and (ii) the optical excitation from the trap is very low [11].
Optical lattices are a central component of many experiments, as they not only trap the atoms, but also determines many properties of the system.

2.1 Trapping of Neutral Atoms

Consider a two level atom in the presence of a time-varying electric field $\boldsymbol{E} = \boldsymbol{\varepsilon} E_0 \exp\{(i(\boldsymbol{k r} - \omega_L t))\}$, where E_0 is its amplitude, $\boldsymbol{\varepsilon}$ is its polarization vector, $\boldsymbol{k}$ is its wave vector and ω_L is its frequency. The interaction between the atom and the electric field causes a perturbation of the atoms energy levels, otherwise known as the AC Stark-shift. The Hamiltonian describing this interaction is

$$\hat{H}_{int} = \hat{d}\boldsymbol{E} , \tag{1}$$

where $\hat{d} = -e\hat{r}$ is the electric dipole operator.
Consider equation (1) as a perturbation to the Hamiltonian of the atom. To first order the non-degenerate, time-independent perturbation of the energy of state i reads $E_i^{(i)} = \langle i| \hat{H}_{int} |i\rangle$. However, only states of opposite parity will contribute to the matrix elements of $\langle \hat{H}_{int} \rangle$, as (1) is linear in space. Thus, all first-order perturbation terms cancel.
To second order the perturbation of state i is given by

$$E_i^{(2)} = \sum_{j \neq i} \frac{| \langle j| \hat{H}_{int} |i\rangle |^2}{\varepsilon_i - \varepsilon_j} . \tag{2}$$

Here, the states $|i\rangle$ and $|j\rangle$ and their corresponding energies, ε_i and ε_j, are of the dressed state picture, where one considers the combined system of the atom and the light field [5]. The state $|i\rangle$ represents the atom being in its ground state, while the light field contains n photons. Thus, the energy of the combined state is $\varepsilon_i = n\hbar\omega_L$, when setting the energy of the atomic ground state to zero. Meanwhile, state $|j\rangle$ is when the atom has been excited by absorbing one of the photons of the field. Hence, the energy of this state is $\varepsilon_j = \hbar\omega_0 + (n-1)\hbar\omega_L$. Defining the detuning $\Delta = \omega_L - \omega_0$ allows writing the perturbation in the form

$$E_{g/e}^{(2)} = \pm \frac{| \langle e| \hat{d} |g\rangle |^2}{\Delta} |E_0|^2, \tag{3}$$

where the upper sign is assigned to the atomic ground state $|g\rangle$. This can be rewritten in order to reflect properties of the atom and the field, by considering the intensity of the light, $I = \frac{1}{2}\epsilon_0 c|\boldsymbol{E}|^2$, and the decay rate of the atom, Γ. Thus, equation (3) can be written as [11]

$$E_{e/g}^{(2)} = \pm \frac{3\pi c^2}{2\omega_0} \frac{\Gamma}{\Delta} I \tag{4}$$

This is the AC-Stark shift, which constitutes the dipole potential. For red detuning ($\Delta < 0$) the ground state will experience a negative shift leading to an attractive potential with depth depending on the intensity of the laser. Similarly, a blue-detuned laser ($\Delta > 0$) will repel the atom. An illustration of this can be seen in figure 1. Since the sign is reversed for the excited state, it is important that the atom remains in the ground state. Thus, one has to minimize the scattering with the optical potential. The scattering rate is given as [11]

$$\Gamma_{sc} = \frac{3\pi c^2}{2\hbar\omega_0^3} \left(\frac{\Gamma}{\Delta} \right)^2 I . \tag{5}$$

As the detuning becomes small, the laser becomes resonant with the atom causing a large increase in scattered photons. Therefore, one has to choose a large detuning in order for the potential to remain
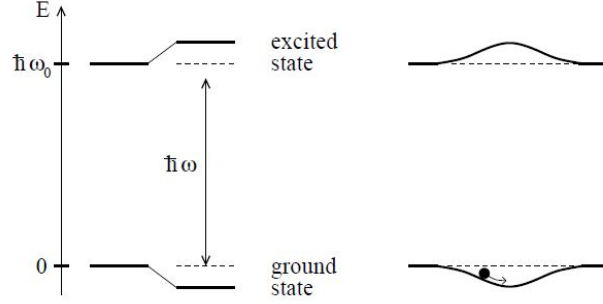
Figure 1: *Light shifts of a two-level atom. Left-hand side, red-detuned light ($\Delta < 0$) shifts the ground state down and the excited state up by same amounts. Right-hand side, a spatially inhomogeneous field like a Gaussian laser beam produces a ground-state potential well, in which an atom can be trapped. Figure and caption are adopted from [11].*

conservative. However, this comes at the cost of a weaker potential. To compensate this, a high laser intensity must be used, in order for the potential to reach sufficient depth. In practise there will be a limit to the laser power available, however, for most alkali-metal atoms the detuning is typically chosen to be large compared to the excited-state hyperfine structure splitting, which provides enough depth while being sufficient to suppress scattering events [3].

2.2 Optical Lattices

The dipole potential in equation (4) scales with the intensity of the laser. Thus, superimposing laser beams allows for creating a multitude of different potentials through the interference patterns of the lasers. A simple standing wave from two counter-propagating light fields will lead to an array of potential wells

$$V(z) = -V_0 \cos^2 kz \ , \tag{6}$$

where $V_0 = |\frac{3\pi c^2}{2\omega_0^3} \frac{\Gamma}{\Delta} 4I_0|$ from equation (4). In practise, a one dimensional lattice like that of equation (6) is created by shining a single laser beam at a mirror, whereby it interferes with itself. Adding another laser beam in a different direction creates a periodic two dimensional potential. For orthogonal polarization of the two lasers, the resulting potential is purely the sum of the sinusoidal standing wave potential, as no interference term is present [24]. Note, that the lattice is only well defined for distances much smaller than the waist of the laser beams, as the lattice is only present within the overlap of the two beams. Various shapes of the lattice can be achieved by adjusting the angle between the beams, however, the most common setup is using two orthogonal beam creating a square lattice of one dimensional tubes, as seen in figure 2. In order to create a three dimensional lattice, as seen in figure 2, an additional third perpendicular laser beam is needed. In the center of the trap, the lattice potential is then given by

$$V(x, y, z) = -V_0 \left(\cos^2 kx + \cos^2 ky + \cos^2 kz \right) \ , \tag{7}$$

for distances much smaller than the beam waist. In addition to the lattice, an external harmonic confinement will be present due to the Gaussian profile of the laser beams [3].

2.3 Band Structure

Consider a periodic potential as described by equation (6). *Bloch's Theorem* states that energy eigenstates of a periodic potential with lattice vector $\boldsymbol{R}$ and quasi-momentum q can be written as Bloch waves, which takes the form

$$\phi_{\boldsymbol{q}}^{(n)}(\boldsymbol{r}) = e^{i\boldsymbol{qr}} u^{(n)}(\boldsymbol{r}) \ , \tag{8}$$
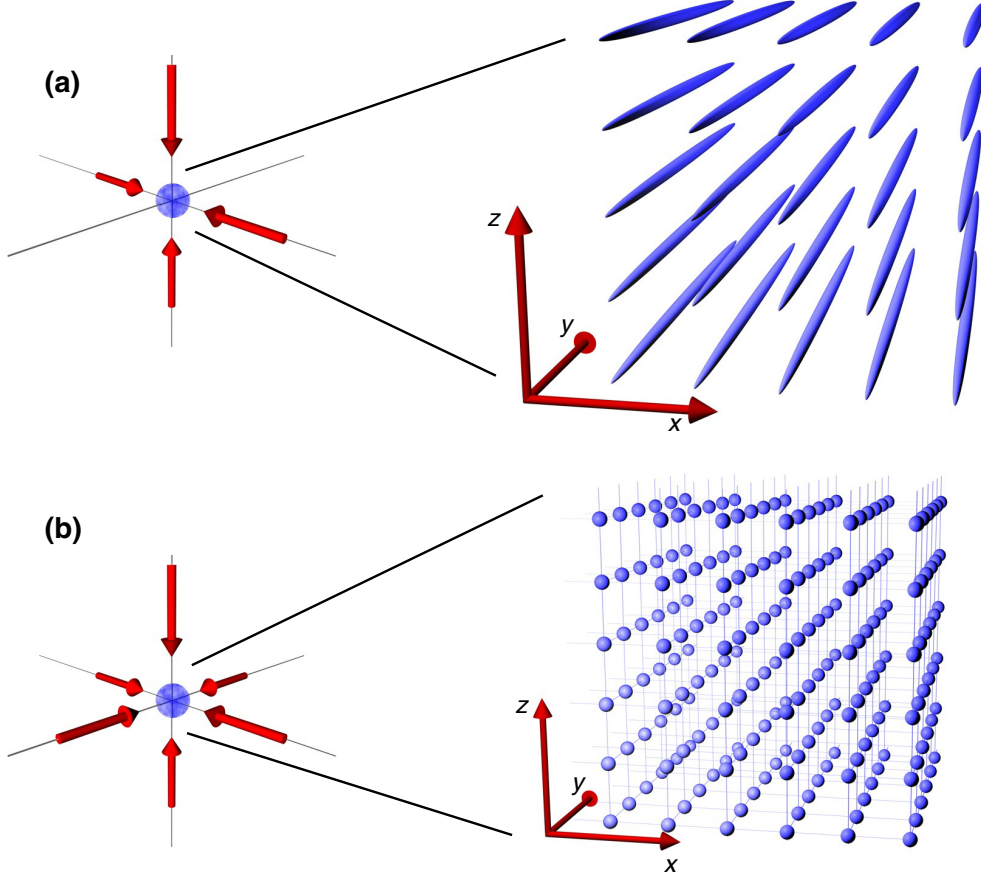
Figure 2: *(a) Two dimensional optical lattice formed by two mutually orthogonal laser beams. These tubes have a characteristic cigar shape, due to the Gaussian profile of the lasers. (b) Upon using three orthogonal laser beams, the result is a three dimensional lattice reminiscent of a cubic crystal. Figure is adopted from [43].*

which is a plane wave modulated by a function with the same periodicity as the potential $u^{(n)}(\boldsymbol{r}) = u^{(n)}(\boldsymbol{r}+\boldsymbol{R})$. Furthermore, the Bloch waves are periodic in reciprocal space, such that $\psi_{\boldsymbol{q}}^{(n)}(\boldsymbol{r}) = \phi_{\boldsymbol{q}+\boldsymbol{G}}^{(n)}(\boldsymbol{r})$, where $\boldsymbol{G}$ is a reciprocal lattice vector. [18]

This leads to an energy spectrum in the shape of bands with the periodicity of the first *Brillouin Zone*. Bands are denoted by the band index n, and their shape is determined by both the shape and the depth of the potential. The potential depth is often denoted in units of the recoil energy $E_r = \frac{\hbar^2 k^2}{2m}$, where m is the mass of the atom, and k is the photon wave number of the light forming the optical lattice. For $V_0 = 0$, the particles are free, hence the bands will be parabolic. Meanwhile, for $V_0 \to \infty$, no interaction between different wells of the lattice can take place, as the wavefunctions of the trapped atoms will be confined to their respective well. Thus, the lattice is reduced to an array of independent harmonic oscillators, whereby the bands will appear flat with equal spacing [10].

2.4 Localized States

For lattice potential depths within $5E_r \leq V_0 \leq 8E_r$, the lattice is in the *tight binding limit*. Within this range, the wavefunctions of the trapped atoms will only overlap with other wells in their closest proximity. Thus, interactions between wells are almost purely of nearest neighbour nature. Due to how well localized the wavefunctions are, a basis of Wannier functions is ideal for describing the system.

Wannier functions are related to Bloch functions through the Fourier transform [19]

$$w^{(n)}(\boldsymbol{r}) = \frac{1}{\sqrt{N_L}} \sum_q e^{-i\boldsymbol{q}\boldsymbol{R}} \phi_{\boldsymbol{q}}^{(n)}(\boldsymbol{r}) \ , \tag{9}$$

where N_L is the number of primitive cells of the lattice. The Wannier functions are well localized and centred around the lattice at site $\boldsymbol{R}$. In the case of a separable periodic potential, like that of equation (7), the single-particle problem becomes dimensional [20]. Lastly, Wannier functions obey the orthonormality relation

$$\int \mathrm{d}^3r \ w^{(n)*}(\boldsymbol{r} - \boldsymbol{R})w^{(n')}(\boldsymbol{r} - \boldsymbol{R'}) = \delta_{n,n'}\delta_{\boldsymbol{R},\boldsymbol{R'}} \ , \tag{10}$$

thus forming a complete basis [3]. Figure 3 shows Wannier functions plotted for lattice potential depths
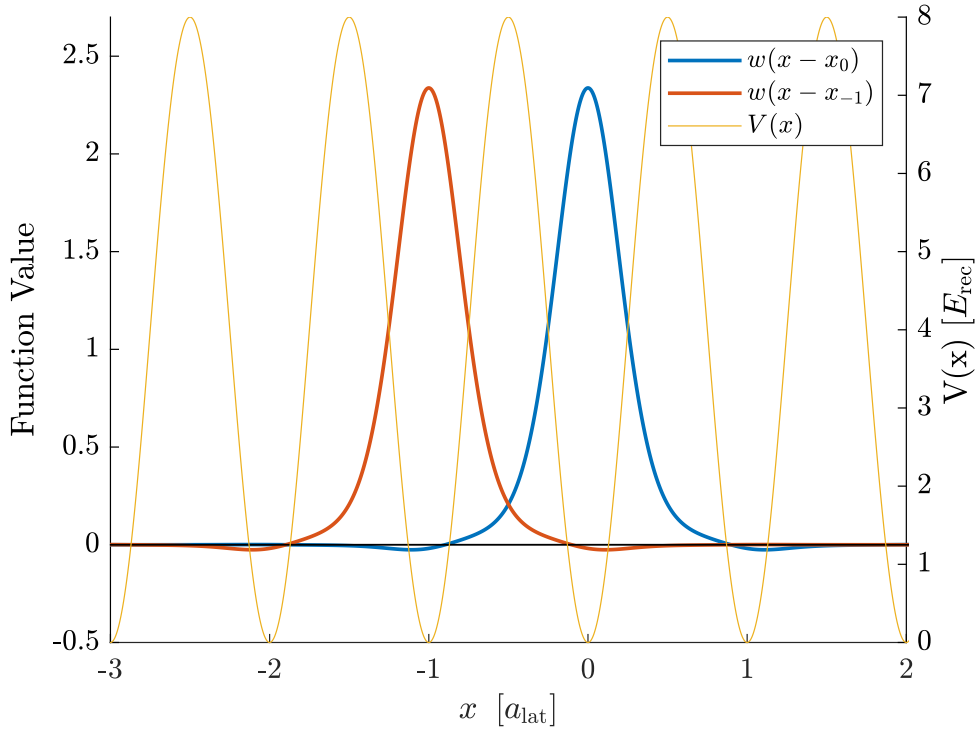
Figure 3: *Two one-dimensional Wannier functions plotted for a lattice potential depth of $V_0 = 8E_r$.*

within the tight binding limit. As evident from the plot, the functions overlap with only their nearest neighbours. In the case of a more shallow lattice, the functions would extends to further wells, while they will tend towards a Gaussian shape as the lattice depth increases [10].

3 Bose-Einstein Condensates

Bosons are particles of integer spin, whose statistics obey those of a Bose-Einstein distribution

$$n_i = \frac{g_i}{\exp\left((\varepsilon_i - \mu)/k_BT\right) - 1} \ , \tag{11}$$

where i denotes the state, n_i is the population of the state, g_i is its degeneracy, ε_i is its energy, μ is the chemical potential, k_B is the Boltzmann constant, and T is the temperature. One important feature of bosons is that, unlike fermions, multiple particles can occupy the same quantum state. At higher temperatures the energy spectrum is practically continues, whereby this property has little effect, as two particles occupying the same single-particle state is highly unlikely. However, at low temperatures the energy spectrum systems often become increasingly discrete, hence the statistics of the particles

becomes very important. As evident from equation (11), the population of the ground state diverges as $T \to 0$. However, even below the finite temperature, T_c, one will observe a macroscopic population of the ground state. T_c is called the critical temperature, and marks the point where multiple particles will start forming a Bose-Einstein Condensate (BEC). [27]

3.1 Non-Interacting Particles

In the case of non-interacting particles and zero temperature, all particles of a Bose gas can be described by identical single-particles wavefunctions $\phi(\boldsymbol{r}_i)$. Hence, the many-body wavefunction is simply given by the product

$$\Psi(\boldsymbol{r}_1, \ldots, \boldsymbol{r}_N) = \prod_i^N \phi(\boldsymbol{r}_i) \,. \tag{12}$$

Such a product state can be described by a single macroscopic wavefunction

$$\psi(\boldsymbol{r}) = \sqrt{N}\varphi(\boldsymbol{r}) \,, \tag{13}$$

where $\phi(\boldsymbol{r})$ is the wave function of the single-particle state, in which the bosons condensate into [26].

Second-Quantization

When describing Bose-Einstein condensates it is very convenient to work in second quantization, which describes the number of particle in each state rather than the state of each particle.

First, consider a basis of single particle states $\{|n\rangle\}$, namely a Fock basis. In this space particles are created or annihilated through their respective operators

$$\hat{a}_\mu^\dagger |0_\mu\rangle = |1_\mu\rangle \,. \tag{14}$$

For bosons the creation and annihilation operators fulfill the commutation relations

$$[\hat{a}_\nu, \hat{a}_\mu] = [\hat{a}_\nu^\dagger, \hat{a}_\mu^\dagger] = 0 \quad, \quad [\hat{a}_\nu, \hat{a}_\mu^\dagger] = \delta_{\nu,\mu} \,, \tag{15}$$

with the number operator given as

$$\hat{n}_\mu = \hat{a}_\mu^\dagger \hat{a}_\mu \,. \tag{16}$$

In second quantization many-body states are described by the occupation of the individual Fock states. Thus, a creation operator will raise the number of particles in its corresponding state by one, while the annihilation operator will lower it:

$$\hat{a}^\dagger |N_0, N_1, \ldots, N_\nu, \ldots\rangle = \sqrt{N_\nu + 1} |N_0, N_1, \ldots, N_\nu + 1, \ldots\rangle \tag{17}$$

$$\hat{a} |N_0, N_1, \ldots, N_\nu, \ldots\rangle = \sqrt{N_\nu} |N_0, N_1, \ldots, N_\nu - 1, \ldots\rangle \,. \tag{18}$$

Likewise, the number operator $\hat{n}_\mu$ will count the number of particles in its corresponding state.

These operators can be combined with an orthonormal basis of spatial wavefunctions $\{\phi_k\}$ in order to create field operators

$$\hat{\psi}(\boldsymbol{r}) = \sum_k \phi_k \hat{a}_k \quad, \quad \hat{\psi}^\dagger(\boldsymbol{r}) = \sum_k \phi_k^* \hat{a}_k^\dagger \,, \tag{19}$$

where $\hat{\psi}(\boldsymbol{r})$ will create a particle at location $\boldsymbol{r}$. For bosons the field operators fulfil the commutation relations [4]

$$\left[\hat{\psi}(\boldsymbol{r}), \hat{\psi}^\dagger(\boldsymbol{r}')\right] = \delta(\boldsymbol{r} - \boldsymbol{r}') \quad, \quad \left[\hat{\psi}(\boldsymbol{r}), \hat{\psi}(\boldsymbol{r}')\right] = 0 \,. \tag{20}$$

Now, consider a gas of non-interacting bosons described by equation (13), where ϵ_k is the energy of the k'th single-particle state. Due to the completeness of the basis of single-particle wavefunctions, $\{\phi_k\}$, the creation operator can be expressed as

$$\hat{a}_k = \int \mathrm{d}^3 r \, \phi_k^*(\boldsymbol{r})\hat{\psi}(\boldsymbol{r}) \,. \tag{21}$$

Using this, the Hamiltonian can be written as

$$\begin{aligned}
\hat{H}^{(0)} &= \sum_k \epsilon_k \hat{a}_k^\dagger \hat{a}_k \\
&= \sum_k \int \mathrm{d}^3 r_1 \mathrm{d}^3 r_2 \; \epsilon_k \phi_k(\boldsymbol{r_1}) \phi_k^*(\boldsymbol{r_2}) \; \hat{\psi}^\dagger(\boldsymbol{r_1}) \hat{\psi}(\boldsymbol{r_2}) \\
&= \int \mathrm{d}^3 r \; \hat{\psi}^\dagger(\boldsymbol{r}) \left(-\frac{\hbar^2}{2m} \nabla^2 + U(\boldsymbol{r}) \right) \hat{\psi}(\boldsymbol{r})
\end{aligned} \tag{22}$$

3.2   Weakly Interacting Particles

A characteristic of a BEC is its low temperature and density. Thus, is it a valid approximation to only consider two-particle interactions

$$\hat{H}^{(2)} = \frac{1}{2} \sum_{i \neq j} V(\boldsymbol{r_i} - \boldsymbol{r_j}) \,. \tag{23}$$

At low energies all interactions can be considered of s-wave nature, because all waves of higher angular momentum are reflected by the centrifugal barrier. Furthermore, for cold gases the thermal de Broglie wavelength is much larger than the effective extension of the interaction potential. Therefore, the actual shape of the scattering potential is irrelevant, hence one can replace it with a pseudo-potential

$$V(\boldsymbol{r} - \boldsymbol{r'}) = g \, \delta(\boldsymbol{r} - \boldsymbol{r'}) = \frac{4\pi\hbar^2 a}{m} \delta(\boldsymbol{r} - \boldsymbol{r'}) \,, \tag{24}$$

which results in the same scattering phase as the real, more complicated scattering potential. Thus, the interaction of cold atoms is fully determined by the scattering length, a [10].
Introducing the density operator

$$\hat{\rho}(\boldsymbol{r}) = \hat{\psi}^\dagger(\boldsymbol{r}) \hat{\psi}(\boldsymbol{r}) \,, \tag{25}$$

allows writing $\hat{H}^{(2)}$ in second quantization

$$\hat{H}^{(2)} = \frac{1}{2} \int \mathrm{d}^3 r_1 \mathrm{d}^3 r_2 V(\boldsymbol{r_1} - \boldsymbol{r_2}) \hat{\psi}^\dagger(\boldsymbol{r_1}) \hat{\psi}(\boldsymbol{r_1}) \left(\hat{\psi}^\dagger(\boldsymbol{r_2}) \hat{\psi}(\boldsymbol{r_2}) - \delta(\boldsymbol{r_1} - \boldsymbol{r_2}) \right) \tag{26}$$

$$= \frac{1}{2} \int \mathrm{d}^3 r_1 \mathrm{d}^3 r_2 \hat{\psi}^\dagger(\boldsymbol{r_1}) \hat{\psi}^\dagger(\boldsymbol{r_2}) V(\boldsymbol{r_1} - \boldsymbol{r_2}) \hat{\psi}(\boldsymbol{r_1}) \hat{\psi}(\boldsymbol{r_2}) \,. \tag{27}$$

Combining this with the basic Hamiltonian of equation (22), gives the full Hamiltonian in second quantization

$$\hat{H} = \hat{H}^{(0)} + \hat{H}^{(2)} \tag{28}$$

$$= \int \mathrm{d}^3 r \; \hat{\psi}^\dagger(\boldsymbol{r}) \left(-\frac{\hbar^2}{2m} \nabla^2 + U(\boldsymbol{r}) \right) \hat{\psi}(\boldsymbol{r}) + \frac{1}{2} \int \mathrm{d}^3 r_1 \mathrm{d}^3 r_2 \; \hat{\psi}^\dagger(\boldsymbol{r_1}) \hat{\psi}^\dagger(\boldsymbol{r_2}) V(\boldsymbol{r_1} - \boldsymbol{r_2}) \hat{\psi}(\boldsymbol{r_1}) \hat{\psi}(\boldsymbol{r_2})$$
$$\tag{29}$$

Using this Hamiltonian to try and solve the Heisenberg equations of motion for the field operators leads to

$$i\hbar \frac{\partial}{\partial t} \hat{\psi}(\boldsymbol{r}) = \left[\hat{\psi}(\boldsymbol{r}) \,, \; \hat{H} \right] = \left(-\frac{\hbar^2}{2m} \nabla^2 + U(\boldsymbol{r}) + g \hat{\psi}^\dagger(\boldsymbol{r}) \hat{\psi}(\boldsymbol{r}) \right) \hat{\psi}(\boldsymbol{r}) \,, \tag{30}$$

which is not solvable in general. However, in the scenario of a BEC the scattering length a is much less than the mean inter-particle distance, such that $na^3 \ll 1$, where n is the density of the gas. In this regime the mean-field approximation is viable

$$\hat{\psi}(\boldsymbol{r}) = \psi(\boldsymbol{r}) + \delta\hat{\psi}(\boldsymbol{r}) \,, \tag{31}$$

where $\psi(\boldsymbol{r})$ is the mean-field given by equation (13), and $\delta\hat{\psi}(\boldsymbol{r})$ is fluctuations from the mean. If $\langle \delta\hat{\psi}(\boldsymbol{r}) \rangle = 0$, the fluctuations can be neglected, leading to the Gross-Pitaevskii equation [12, 28]

$$i\hbar \frac{\partial}{\partial t} \hat{\psi}(\boldsymbol{r}) = \left(-\frac{\hbar^2}{2m} \nabla^2 + U(\boldsymbol{r}) + g|\psi(\boldsymbol{r})|^2 \right) \psi(\boldsymbol{r}) \,. \tag{32}$$

The Gross-Pitaevskii equation is very similar to the Schrödinger equation with exception of the non-linear term $g|\psi(\boldsymbol{r})|^2$, which can make the equation hard to solve in regions of low density.

4 Bose-Hubbard Model of Interacting Bosons in a Lattice

The Bose-Hubbard model describes weakly interacting bosons in a periodic lattice within the tight binding limit. The model is perfectly capable of predicting results with good accuracy, however, two conditions must hold in order for the it to be valid: (i) both the thermal energy and the mean interaction energy at a single site must be much smaller than the separation to first excited band, $\hbar\omega_0$, and (ii) the Wannier functions decay essentially within the length of the lattice constant [3].

Under these conditions one is assured that only the lowest band is taken into account, and that only nearest-neighbour interactions take place.

The Bose-Hubbard model is interesting, as it supports two distinct phases: the Superfluid phase and the Mott-Insulator phase. Furthermore, the model contains effects such as a quantum phase transition between the two phases mentioned above, which can be crossed without any change in external parameters.

4.1 The Bose-Hubbard Hamiltonian

Consider the Hamiltonian for bosonic particles in a trapping potential (described by equation (29)) in one dimension. For a periodic lattice potential in the tight binding limit it is favourable to work in a basis of localized Wannier functions. Expanding the field operators of the Hamiltonian in equation (29) in the Wannier basis yields [15]

$$\hat{H} = \int \mathrm{d}x \sum_{ij} w^*(x - x_i)\hat{a}_i^\dagger \left(-\frac{\hbar^2}{2m}\nabla^2 + V(x)\right) w(x - x_j)\hat{a}_j$$

$$+ g \int \mathrm{d}x \sum_{ijkl} w^*(x - x_i)w^*(x - x_j)w(x - x_k)w(x - x_l)\hat{a}_i^\dagger \hat{a}_j^\dagger \hat{a}_k \hat{a}_l \tag{33}$$

$$= -\sum_{ij} J_{ij}\hat{a}_i^\dagger \hat{a}_j + \sum_{ijkl} U_{ijkl}\hat{a}_i^\dagger \hat{a}_j^\dagger \hat{a}_k \hat{a}_l \ , \tag{34}$$

where

$$J_{ij} = -\int \mathrm{d}x \ w^*(x - x_i) \left(-\frac{\hbar^2}{2m}\nabla^2 + V(x)\right) w(x - x_j) \tag{35}$$

$$U_{ijkl} = g \int \mathrm{d}x \ w^*(x - x_i)w^*(x - x_j)w(x - x_k)w(x - x_l) \tag{36}$$

Since the system is periodic, one can consider a single site, $i = 0$, as representative for the entire lattice. In this way, the different terms of the Hamiltonian can be interpreted as follows:

$$J_{00} = \text{constant energy offset}$$
$$J_{01} = \text{"overlap matrix element" to neighbouring site}$$
$$J_{02-0\infty} = \text{"overlap matrix element" to further sites}$$
$$U_{0000} = \text{on-site interaction for two particles}$$
$$U_{0ii0} = \text{interaction off-site}$$
$$U_{0001} = \text{interaction + tunnelling , off-site}$$

Due to the rapid decay of the Wannier functions, the overlap of wavefunctions is limited to their nearest neighbour. Dropping all exponentially suppressed terms and constant offsets yields the Bose-Hubbard Hamiltonian

$$\hat{H} = -J \sum_{\langle i,j \rangle} \hat{a}_i^\dagger \hat{a}_j + \frac{U}{2} \sum_i \hat{n}_i \left(\hat{n}_i - 1\right) + \sum_i \varepsilon_i \hat{n}_i \ , \tag{37}$$

where $J = J_{01}$, $\langle i, j \rangle$ only counts neighbouring pairs, and

$$U = U_{0000} = g \int \mathrm{d}x \; |w(x)|^4 \; . \tag{38}$$

The first term of the Bose-Hubbard Hamiltonian describes the kinematics within the model, which takes the form of tunneling between neighbouring sites. This is interpreted by annihilating a particle at site j while creating a particle at site i. The second term describes the interaction between particles within a single site, and the last term $\sum_i \varepsilon_i \hat{n}_i$ takes into account a possible potential offset at different sites.

4.2 Phases of the Bose-Hubbard Model

The Bose-Hubbard model supports two quantum phases: The *Superfluid* phase and the *Mott Insulator* phase. These phases depend on the ratio J/U, and can be described separately by examining the ground state of the Bose-Hubbard Hamiltonian in the two extreme limits of the J/U ratio.

Superfluid Phase

For a system where the tunneling matrix element J is dominant, the lowest energy is obtained by delocalizing the atoms over the entire lattice. Thereby the wavefunction will be a product over single-particle states, and the system will be a superfluid [10].
Consider the case of negligible interactions and a lattice of equal depth. In this scenario the Bose-Hubbard Hamiltonian reduces to

$$\hat{H} = \hat{H}_J = -J \sum_{\langle i,j \rangle} \hat{a}_i^\dagger \hat{a}_j \; , \tag{39}$$

which is completely periodic within the lattice due to the lack of site specific terms. This leads to solutions in the shape of Bloch waves. The Fourier transform of the annihilation and creation operators

$$\hat{a}_j = \frac{1}{N_L} \sum_q e^{iqx_j} \hat{a}_q \quad , \quad \hat{a}_j^\dagger = \frac{1}{N_L} \sum_q e^{-iqx_j} \hat{a}_q^\dagger \tag{40}$$

allows for writing the Hamiltonian (39) in momentum space

$$\hat{H}_J = -J \sum_{q=-\infty}^{\infty} \left(e^{-iqd} + e^{ikd} \right) \hat{n}_q \; , \tag{41}$$

where d is the lattice distance. In momentum space the Hamiltonian is diagonal and results in a continuous energy spectrum

$$E_q = -2J \cos(qd) \; . \tag{42}$$

Thus, the excitation spectrum of the Superfluid is said to be gapless.

The lowest energy is of the system is obtained for $q = 0$, whereby the ground state is

$$|\Psi_{SF}\rangle = \frac{1}{\sqrt{N!}} \left(\hat{a}_{q=0}^\dagger \right)^N |0\rangle = \frac{1}{\sqrt{N!}} \left(\frac{1}{N_L} \sum_{j=1}^{N_L} \hat{a}_j^\dagger \right)^N |0\rangle \; , \tag{43}$$

where N is the number of particles. This state supports a well defined macroscopic phase on each lattice site, since the many-body state is a product over identical single-particle states [10]. With all particle condensed into the $q = 0$ momentum space state, the particles are completely de-localized in real space, which can be seen by taking the Fourier transform. For large $N, N_L \to \infty$ at fixed density N/N_L the state becomes indistinguishable from having coherent states, $|\alpha\rangle$, on all lattice sites [3]

$$|\Psi_{SF}\rangle \approx \prod_j \left(e^{\sqrt{N/N_L} \hat{a}_j^\dagger} \right) |0\rangle = |\alpha_1\rangle \otimes |\alpha_2\rangle \otimes \ldots \tag{44}$$
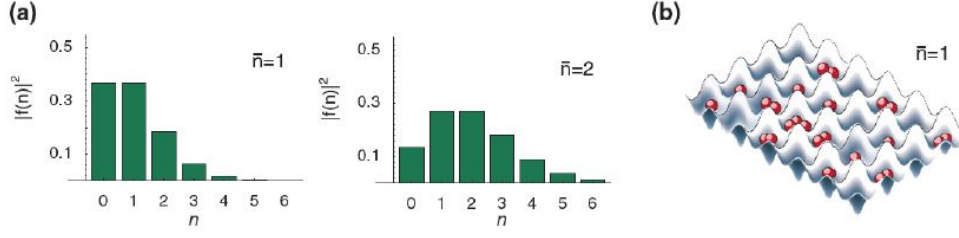
Figure 4: *(a) The statistics for the number of particles per lattice site n for a filling fraction of $\bar{n} = 1$ and $\bar{n} = 2$ in the superfluid phase. (b) Illustration of the particles in the lattice. There will be large fluctuations of the number of particles found at each lattice site at a given time. Figure and caption adopted from [10].*

Since bosonic operators at different sites commute, the superfluid state can be factorized into a product of local coherent states. Coherent states are eigenstates of the annihilation operator $\hat{a} |\alpha\rangle = \alpha |\alpha\rangle$, where $|\alpha|^2$ can be considered the particle density of the system, and $\alpha = |\alpha|e^{i\phi}$, with ϕ being a global phase. Utilizing the coherent state form of the wavefunction (eq. (44)) the average filling fraction $\bar{n}$ can be calculated

$$\bar{n} = \langle \hat{n}_i \rangle = \langle \Psi_{SF} | \hat{a}_j^\dagger \hat{a}_j | \Psi_{SF} \rangle = \frac{N}{N_L} , \tag{45}$$

as well as the fluctuations of particle number per site

$$\frac{\sqrt{\Delta \bar{n}^2}}{\bar{n}} \sim \frac{1}{\sqrt{\bar{n}}} . \tag{46}$$

Therefore, the probability distribution for the number of atoms at a given site is Poissonian, which can be seen in figure 4. Due to the relatively large fluctuation of particle number per site, one would find a somewhat random number of atoms at a given site in a measurement. In the presence of a finite interaction, U, the resulting distribution would be sub Poissonian due to number squeezing [10].

Mott-Insulator Phase

In the case of negligible tunneling, only the on-site interaction between the atoms has to be taken into account, and the Bose-Hubbard Hamiltonian reduces to

$$\hat{H} = \hat{H}_U = \frac{U}{2} \sum_i \hat{n}_i (\hat{n}_i - 1) , \tag{47}$$

which is quadratic in $\hat{n}_i$. This heavily penalizes having multiple particles at the same site. Thus, the ground state of the system will be an equal distribution of all the particles throughout the lattice. Any fluctuations from this average will increase the energy, whereby the phase is said to be incompressible [9]. This incompressibility can be formulated as $\frac{\partial n}{\partial \mu} = 0$, where μ is the chemical potential, and is the defining property of the Mott-Insulator [3].

Consider the case $\bar{n} = 1$, (average filling of one particle per site). This can be described by a state with a single particle located on each site [3]

$$|\Psi_{Mott}\rangle = \prod_j \hat{a}_j^\dagger |0\rangle . \tag{48}$$

This is a simple product of local Fock states with precisely one atom per site, which is illustrated in figure 5. This is the configuration of atoms, which minimizes the energy with regards to the Hamiltonian of eq. (47). Any fluctuation from unit occupancy will increase the energy, as merely a single double occupancy will increase the energy by U. Thereby, unlike the energy spectrum of the Superfluid, the Mott-Insulator spectrum is gapped. As long as the gain in kinetic energy due to hopping, J, is smaller than the on-site interaction, U, the atoms remain localized. However, for $J > 0$ the ground state is no longer a the simple product state described in eq. (48) [3]. As J increases, the
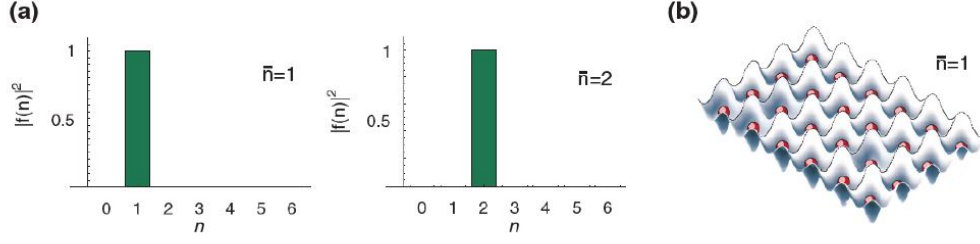
Figure 5: *(a)The statistics for the number of particles per lattice site n in the Mott-insulator phase, for a filling fraction of $\bar{n} = 1$ and $\bar{n} = 2$. (b) Illustration of the particles in the lattice. The particles does not hop around in the lattice and are equally distributed. Caption and figure are adapted from [10].*

gap in the excitation spectrum will gradually decrease until the transition to the superfluid is reached and the spectrum becomes gapless.

While the Mott-Insulator phase has complete localization, the phases on the individual sites have obtained maximum uncertainty. Therefore, no phase coherence between different sites is present [10].

4.3   Phase Transition

Consider once again the full Bose-Hubbard Hamiltonian (37). The superfluid and the Mott-Insulator account for the two limits of the ratio J/U, however, it order to understand the full phase diagram of the Bose-Hubbard model one has to derive the U_{crit} for which the phase transition occurs. There are several ways of doing this - one of them is looking at a mean-field solution of the Bose-Hubbard model. For simplicity the scenario $T = 0$ is treated here. Even without a change of temperature the phase transition still happens, hence the label *quantum phase transition* referring to the fact that the phase transition can happen without change of external parameters [30].

Applying the mean field approximation to the annihilation operator yields

$$\hat{a}_j = \psi + \delta\hat{a}_j \ , \tag{49}$$

where ψ is the locally constant mean field, and $\delta\hat{a}_j$ is the fluctuation term. Inserting this into the Hamiltonian yields

$$\hat{H}_{MF} = -J \sum_{\langle i,j \rangle} \left(\psi^* + \delta\hat{a}_i^\dagger \right) (\psi + \delta\hat{a}_j) + \text{int.} \tag{50}$$

Instead of considering the Hamiltonian as a whole, it can be considered as a sum of local on-site Hamiltonians

$$\hat{H}_{MF} = \sum_i \hat{h}_i \ . \tag{51}$$

For a homogeneous system $\hat{h}_i = \hat{h}_j \ \forall i, j$. One can write the kinetic part of the Hamiltonian locally if one assumes small fluctuations from the mean field

$$
\begin{aligned}
\hat{a}_i^\dagger \hat{a}_j &= \left(\psi^* + \delta\hat{a}_i^\dagger \right) (\psi + \delta\hat{a}_j) \\
&= \psi^*\psi + \psi^*\delta\hat{a}_j + \psi\delta\hat{a}_i^\dagger + \delta\hat{a}_i^\dagger \delta\hat{a}_j \\
&\approx \psi^*\psi + \psi^* \left(\hat{a}_j - \psi \right) + \psi \left(\hat{a}_i^\dagger - \psi^* \right) \\
&= \psi^*\hat{a}_j + \psi\hat{a}_i^\dagger - \psi^*\psi
\end{aligned} \tag{52}
$$

Since every term only contains a single index, one can let $j \to i$ leaving a local description

$$\hat{h}_i = Jz\psi^*\psi - Jz \left(\psi^*\hat{a}_i + \psi\hat{a}_i^\dagger \right) + \frac{U}{2}\hat{n}_i (\hat{n}_i - 1) + \mu_i\hat{n}_i \ , \tag{53}$$

where z is the number of neighbours of site i [38]. The last term added is a chemical potential, which is needed due to the lack of a fixed particle number locally prompting the use of a Grand Canonical

Ensemble description.

Landau theory is a general theory regarding phase transitions, which states that in the vicinity of a critical point, one may expand the free energy in a power series of some order parameter m. Thus, in order to find U_{crit}, equation (53) must be minimized. In this case this order parameter is the mean field, hence

$$E_{MF} = \text{const.} + a|\psi|^2 + b|\psi|^4 + \ldots \tag{54}$$

Plotting this yields an effective potential, seen in figure 6, which dictates certain properties of the system.
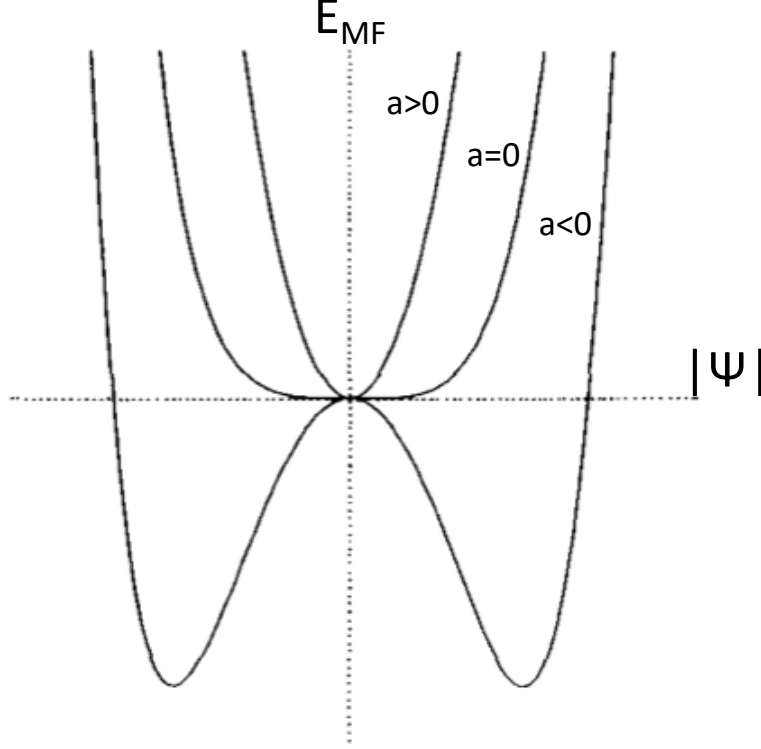
Figure 6: *Effective potential as function of the order parameter ψ. For $a < 0$ the properties of the potential change from having a single, central minimum to having two separated minima. This is an example of spontaneous symmetry breaking associated with a phase transition. [29]*

The potential is symmetric in the complex plane allowing the system to have any phase. Furthermore, at some critical value of a, (here $a = 0$), the potential will shift from having a single central minimum to having minima at some $|\psi|$. This is a U(1) spontaneous symmetry breaking, which in Landau theory is associated with a phase transition [29]. Thus, one need to compute the parameter a of equation (54). One method is using second order perturbation theory, where the $\hat{\psi} = 0$ case is solved exactly, followed by adding a small $\hat{\psi}$ as a perturbation

$$\hat{h}_i^{(0)} = Jz\left(\psi^*\psi\right) + \frac{U}{2}\hat{n}_i\left(\hat{n}_i - 1\right) - \mu\hat{n}_i . \tag{55}$$

Since the zero-order solution only contain number operators, the ground state of the solution can be expressed in the Fock basis:

$$
\begin{aligned}
|0\rangle \quad &\text{for} \quad \mu < 0 \\
|1\rangle \quad &\text{for} \quad 0 \leq \mu < U \\
|2\rangle \quad &\text{for} \quad U \leq \mu < 2U \\
&\vdots
\end{aligned}
$$

Adding on the first order perturbation to the energy

$$E_i^{(1)} = \langle n | \, \delta \hat{a}_i \, | n \rangle = 0 \, , \tag{56}$$

yields nothing, thus requiring the use of a second order perturbation

$$E_i^{(2)} = \sum_{n \neq g} \frac{|\langle n | \, \delta \hat{h}_i \, | g \rangle |^2}{E_g^{(0)} - E_n^{(0)}} \, . \tag{57}$$

Here the perturbation Hamiltonian

$$\hat{h}_i = -zJ \left(\hat{a}_i \psi^* + \psi \hat{a}_i^\dagger \right) \tag{58}$$

contains only single creation/annihilation operators, whereby

$$\langle n | \, \delta \hat{h}_i \, | g \rangle = 0 \quad \text{for} \quad |n - g| \neq 1 \, . \tag{59}$$

Hence, for each annihilation and creation operator only two matrix elements will give a contribution

$$\langle n | \, \hat{a}_i^\dagger \, | n - 1 \rangle = \sqrt{n} \, \langle n | n \rangle$$
$$\langle n + 1 | \, \hat{a}_i^\dagger \, | n \rangle = \sqrt{n + 1} \, \langle n | n \rangle$$
$$\vdots$$

With this the second order perturbation energy reduces to

$$E_i^{(2)} = (Jz)^2 \, |\psi|^2 \left(\frac{n}{E_g^{(0)} - E_{n-1}^{(0)}} + \frac{n + 1}{E_n^{(0)} - E_{n+1}^{(0)}} \right)$$
$$= (Jz)^2 \, |\psi|^2 \left(\frac{n}{U(n - 1) - \mu} + \frac{n + 1}{\mu - Un} \right) \, . \tag{60}$$

Since a is the pre-factor of all terms proportional $|\psi|^2$, collecting those across from all the perturbations yields the approximation

$$a = Jz + (Jz)^2 \, |\psi|^2 \left(\frac{n}{U(n - 1) - \mu} + \frac{n + 1}{\mu - Un} \right) \, . \tag{61}$$

As stated earlier U_{crit} can be found from $a = 0$:

$$0 \overset{!}{=} 1 + \frac{n}{\bar{U}(n - 1) - \bar{\mu}} + \frac{n + 1}{\bar{\mu} - \bar{U} n} \, , \tag{62}$$

with $\bar{\mu}u = \frac{\mu}{Jz}$ and $\bar{U} = \frac{U}{Jz}$. Finally, the solution for the chemical potential is [38]

$$\bar{\mu}u_\pm = \frac{1}{2} \left(\bar{U}(2n - 1) \pm \frac{1}{2} \sqrt{\bar{U}^2 - 2\bar{U}(2n + 1)} \right) \, . \tag{63}$$

Understanding this result can be done be examining figure **??**, which displays a phase diagram of the Bose-Hubbard model. The $\mu_\pm$ curves encloses the region where the system is in the Mott Insulating phase. $(1/\bar{U})_{crit} = (J/U)_{crit}$ can be read off the graph from the point, where the two curves $\mu_\pm$ meet. As mentioned earlier, no fluctuations take place in the Mott Insulator, whereby the particle number per site is well defined, while it for the superfluid can take many values. As the chemical potential increases each site can accommodate more particles as long as the increase in chemical potential compensates the increased energy due to interactions between the particles.

The mean-field solution of the Bose-Hubbard model is only an approximation, which proves quite inaccurate for one dimension. This is seen when comparing the critical ratio for the mean-field approach, $(U/J)_{crit}^{MF,1D} = 11.66$, with numerical results computed using the DMRG method, $(U/J)_{crit}^{DMRG,1D} = $
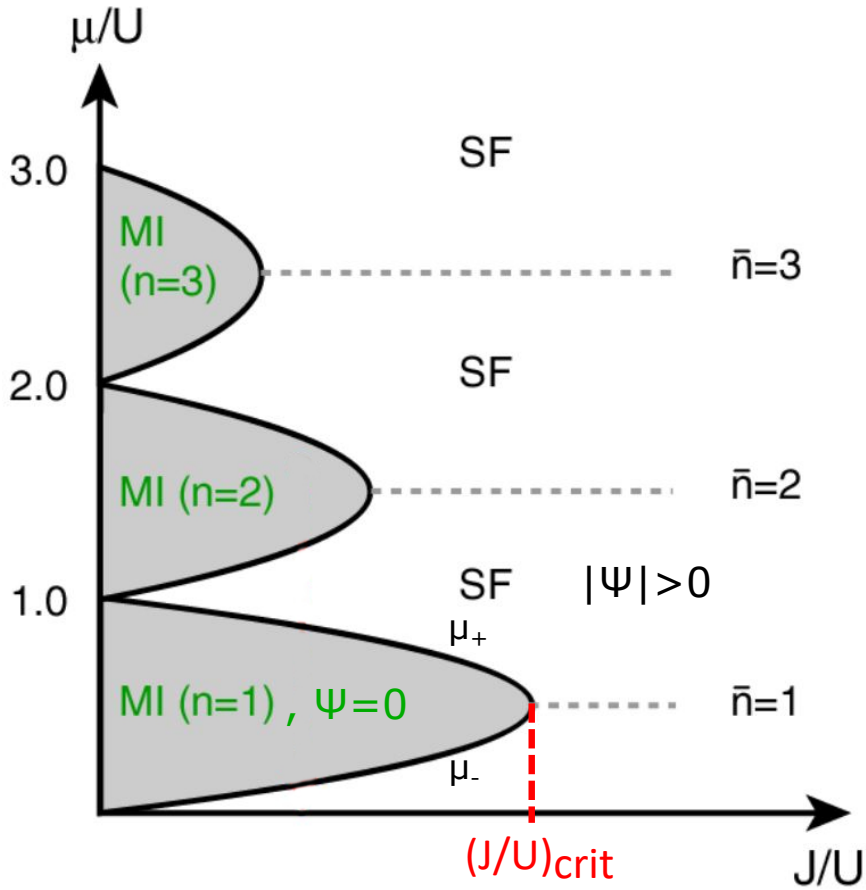
Figure 7: *Phase diagram of Bose-Hubbard model for T = 0. Grey areas mark the Mott Insulator phase for different number of particles per site, while white regions mark the superfluid phase. [10]*

3.37, [22]. Nevertheless, it gives a good intuitive feeling of the physics taking place and how one can describe them without resorting to diagonalizing the Hamiltonian.

5 Matrix Product States

Matrix product states is a parametrization of one dimensional states, which only considers the relevant part of the full Hilbert space, thus greatly simplifying numerical computations within the system. The main idea is to parametrize the coefficients of a general linear combination of states as a product of matrices, with a single matrix for each physical site.

SKRIV INTRO OM MPS MED REFERENCER TIL LITTERATUR - quick "history" * known for a long time * algorithms standardised by White - why do we need MPS description? (copy from numerics chapter) * Do quick analysis of size of Hilbert space * mention efficient application of operators - usage of MPS (mention DMRG and tDMRG here)

5.1 Entanglement in Quantum Systems and Area Laws

Entanglement is a fundamental property of quantum mechanics responsible for correlating different degrees of freedom within a quantum system. Thus, the individual parts of a quantum system can not be described alone, as entanglement with the remainder of the system has to be taken into consideration. This drastically complicates any description of the system, which is why exact descriptions of many-body systems are almost impossible. CITE

The measure of entanglement within a quantum many-body system is the entanglement entropy,

although it is often more instructive to look at the bipartite entanglement entropy, which measures the entanglement between two partitions of the system. Consider a bipartition of the Hilbert space $\mathcal{H} = \mathcal{H}_A \otimes \mathcal{H}_B$. A state $|\psi\rangle \in \mathcal{H}$ can be decomposed using the *Schmidt decomposition* as

$$|\psi\rangle = \sum_\alpha \Lambda_\alpha |\alpha\rangle_A \otimes |\alpha\rangle_B \ , \tag{64}$$

where the states $\{|\alpha\rangle_{A(B)}\}$ form an orthonormal basis of $\mathcal{H}_{A(B)}$, and $\Lambda_\alpha \geq 0$ are the Schmidt coefficients fulfilling $\sum_\alpha \Lambda_\alpha^2 = 1$ CITE. If only one term contributes to the Schmidt decomposition, the state is obviously a product state i.e. the two parts of the Hilbert space are not mutually entangled. More terms, on the other hand, implies that the state is entangled. From the Schmidt decomposition one can determine the reduced density matrix

$$\rho_A = \mathrm{Tr}_B |\psi\rangle \langle\psi| = \sum_\alpha \Lambda_\alpha^2 |\alpha\rangle_A \langle\alpha|_A \ . \tag{65}$$

From this one can determine the entanglement entropy of the chosen bipartition, which is defined as the von-Neumann entropy, S, of the reduced density matrix given by CITE

$$S = -\sum_\alpha \Lambda_\alpha^2 \log \Lambda_\alpha^2 \ . \tag{66}$$

Quite often, one is not conserned with the actual entanglement entropy of the system, but rather how it scales when the region in question grows in size. It is natural to assume that the entanglement entropy scales with the systems size, the *volume* of the system, since this is the case for thermal systems. However, ground states of quantum many-body systems often follow an *area law*, meaning that the scaling of the entropy is linear in the boundary area of the region. This is especially the case for systems with a gapped and local Hamiltonian [7].

In a one dimensional lattice the boundary of a bipartition consists of only one site. Hence, the entropy will be bounded by a constant independent of the size of both the system and the subsystem, if the system follows an area law. This can be understood intuitively, as only degrees of freedom within the correlation length, ξ, of the boundary will be entangled, no matter where in the system the boundary is present [?].

This observation is the key to the success of numerical computations for one-dimensional systems, as one only has to consider a small region of the Hilbert space when performing a variational search for the ground state. A highly efficient way of describing one dimensional systems is through Matrix Product States (MPS), which follow an area law by default, as they are constructed through a series of Schmidt decompositions.

Singular Value Decomposition (SVD)

A central tool for parametrizing a state as an MPS is the *singular value decomposition*. An arbitrary matrix, A, of dimensions $(M \times N)$ can be decomposed into three matrices as

$$A = USV^\dagger \ , \tag{67}$$

where each of the matrices contains unique properties [?]:

- U is of dimension $(M \times \min(M, N))$ and has orthonormal columns, meaning $U^\dagger U = I$. If $M \leq N$ then it is also unitary $UU^\dagger = I$.

- S is a positive, diagonal $(\min(M, N) \times \min(M, N))$ matrix. The diagonal elements are are singular values, and the number of non-zero entries is the Schmidt rank of A.

- $V^\dagger$ is of dimension $(\min(M, N) \times N)$ and has orthonormal rows, meaning $V^\dagger V = I$. If $M \geq N$ then it is also unitary $VV^\dagger = I$.

These properties are very important when building the MPS. Figure 8 shows how this is displayed using diagrams.
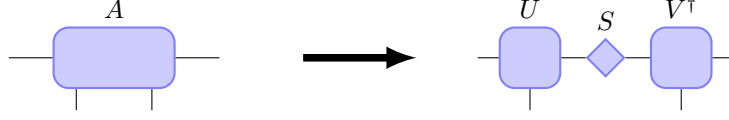
Figure 8: *SVD of a tensor A shown diagrammatically.*

5.2   Construction of an MPS

Matrix products states are parametrisations of one dimensional quantum states through a product of tensors. This parametrisation is especially intuitive for lattice systems, as each lattice site can be represented by a single tensor. These tensors have two different kinds of indices; *physical indices*, j, which corresponds to the physical states at a given site, and *bond indices*, which serves to connect neighbouring sites. Tensors can be merged by contracting the bond connecting them, which is achieved by summing over their common index. Hence, equations involving matrix product states tend to grow quite long, whereby they often are described through diagrams. In the diagrammatic representation the physical indices are marked by vertical legs, while bond indices are marked by horisontal legs. When two tensors are connected by a leg, it means that the corresponding bond is contracted. Further details and examples regarding tensor diagrams can be found in A.

Consider a chain of N sites with each site having a d-dimensional local Hilbert space $\{|j_n\rangle\}$, where $n = 1, \ldots, N$. Thus, an arbitrary quantum state of this system reads

$$|\psi\rangle = \sum_{j_1, \ldots, j_N} c_{j_1 \ldots j_N} |j_1, \ldots, j_N\rangle \ . \tag{68}$$

This description of a general state can be parametrised to the MPS form by applying successive Schmidt decomposition. However, in practice this is done through Singular Value Decompositions (SVD), as these are faster to perform numerically. The two approaches are equivalent, as the singular value decomposition is essentially a restatement of the Schmidt decomposition CITE. Through an SVD, an arbitrary matrix, A, of dimensions $(M \times N)$ can be decomposed into three matrices

$$A = USV^\dagger \ . \tag{69}$$

These matrices have the following properties [**?**]:

- U is of dimension $(M \times \min(M, N))$ and has orthonormal columns, meaning $U^\dagger U = I$. If $M \leq N$, then it is also unitary $UU^\dagger = I$.

- S is a positive, diagonal $(\min(M, N) \times \min(M, N))$ matrix. The diagonal elements are singular values, and the number of non-zero entries is the Schmidt rank of A.

- $V^\dagger$ is of dimension $(\min(M, N) \times N)$ and has orthonormal rows, meaning $V^\dagger V = I$. If $M \geq N$, then it is also unitary $VV^\dagger = I$.

From the general state of eq. (68) an MPS can be constructed through the following steps:

1. The d^N-dimensional vector $c_{j_1 \ldots j_N}$ is reshaped into a $(d \times d^{N-1})$ matrix $\Psi_{j_1, (j_2 \ldots j_n)}$. Performing an SVD on Ψ yields

$$c_{j_1 \ldots j_N} = \Psi_{j_1, (j_2 \ldots j_n)} = \sum_{\alpha_1}^{d} U_{j_1, \alpha_1} S_{\alpha_1, \alpha_1} (V^\dagger)_{\alpha_1, (j_2 \ldots j_N)} = \sum_{\alpha_1}^{d} A_{\alpha_1}^{j_1} \Psi_{(\alpha_1 j_2), (j_3 \ldots j_N)} \ , \tag{70}$$

where U has been decomposed into d row vectors A^{j_1} with entries $A_{\alpha_1}^{j_1} = U_{j_1, \alpha_1}$. In this notation $A_{\alpha_1}^{j_1}$ is a tensor with physical indices j_1 and bond indices α_1. Furthermore, S and $V^\dagger$ has been multiplied and reshaped into a $(d^2 \times d^{N-2})$ matrix, $\Psi_{(\alpha_1 j_2), (j_3 \ldots j_N)}$.

2. The new matrix $\Psi_{(\alpha_1 j_2),(j_3...j_N)}$ is subjected to an SVD decomposition

$$c_{j_1...j_N} = \sum_{\alpha_1}^{d} \sum_{\alpha_2}^{d^2} A_{\alpha_1}^{j_1} U_{(\alpha_1 j_2),\alpha_2} S_{\alpha_2,\alpha_2} (V^\dagger)_{\alpha_2,(j_3...j_N)} = \sum_{\alpha_1}^{d} \sum_{\alpha_2}^{d^2} A_{\alpha_1}^{j_1} A_{\alpha_1,\alpha_2}^{j_2} \Psi_{(\alpha_2 j_3),(j_4...j_N)} , \quad (71)$$

where U has been decomposed into d matrices A^{j_2} with entries $A_{\alpha_1,\alpha_2}^{j_2} = U_{(\alpha_1 j_2),\alpha_2}$. The matrix $\Psi_{(\alpha_2 j_3),(j_4...j_N)}$ has dimensions $(d^3 \times d^{N-3})$ and is yet again a product of the matrices S and $V^\dagger$ from the SVD.

3. This pattern of applying and SVD to the matrix, replacing U, and reshaping into a new matrix is continued throughout the chain leaving

$$c_{j_1...j_N} = \sum_{\alpha_1,...,\alpha_{N-1}} A_{\alpha_1}^{j_1} A_{\alpha_1,\alpha_2}^{j_2} \ldots A_{\alpha_{N-2},\alpha_{N-1}}^{j_{N-1}} A_{\alpha_{N-1},\alpha_N}^{j_N} = A^{j_1} A^{j_2} \ldots A^{j_{N-1}} A^{j_N} , \quad (72)$$

where the sum can be recognized as a matrix multiplication allowing a neater notation.
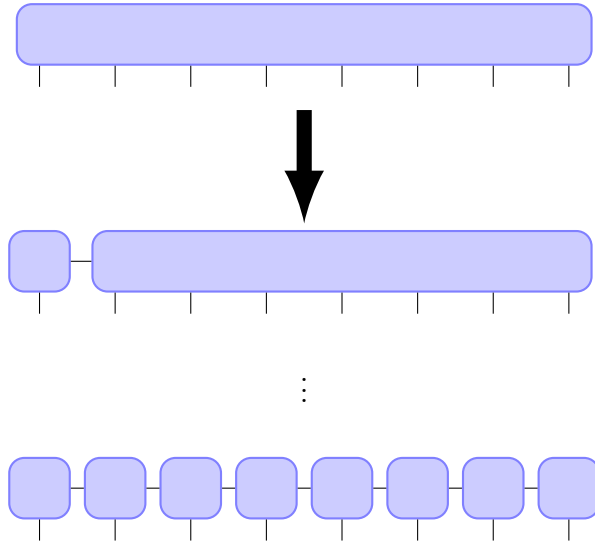
Figure 9: *Diagrammatic representation of the construction of a left-canonical MPS from an arbitrary quantum state through successive SVD's.*

The construction of an MPS is illustrated in figure 9. Thereby, the original state (equation 68) can be written as a matrix product state in the form [**?**]

$$|\psi\rangle = \sum_{j_1,...,j_N} A^{j_1} A^{j_2} \ldots A^{j_{N-1}} A^{j_N} |j_1,\ldots,j_N\rangle . \quad (73)$$

It is worth examining the properties of this representation. From the dimensions of the components of an SVD, one will notice the dimensions of the matrices A^{j_n} follow a pyramid-like structure $(1 \times d), (d \times d^2), \ldots, (d^{N/2-1} \times d^{N/2}), (d^{N/2} \times d^{N/2-1}), \ldots, (d \times 1)$, where N is taken as even for simplicity. Hence, the matrix dimensions increase exponentially making exact computations practically impossible. However, certain simplifications can be made, which greatly reduces computational time without sacrificing much precision. First, one only needs to keep the non-zero, singular values of the matrices S, thus reducing the dimensional factor from d to r_n, where $r_n \leq d$ is the Schmidt rank of the n'th decomposition. Secondly, as discussed earlier, only a few terms is needed to accurately describe entanglement across bonds. Therefore, the matrices S, U and V can be truncated, by keeping only the D largest singular values, as these contribute the most to the state. Thus, the dimension of the matrices will cap at D: $(1 \times d), (d \times d^2), \ldots, (d^n \times D), (D \times D), \ldots, (D \times d^n) \ldots (d \times 1)$, avoiding the otherwise exponential dimensional growth [33]. The amount of singular values needed to be kept in order to produce an accurate approximation of the state is highly dependent of the system. Thus, one often need to perform the same calculation for various values of D, in order to gauge how much the matrices can be truncated.

5.3 Canonical Forms

The MPS described in equation 73 is not unique, as writing

$$\tilde{A}^{j_n} = X_{n-1} A^{j_n} X_n^{-1} \tag{74}$$

describes the same state using different matrices. This gauge freedom allows expressing the MPS in whichever way is most convenient, often resulting in a much lower numerical cost of operations. By choosing a gauge, the MPS is brought into a *canonical form* [39].

**Left-canonical matrix product state**

The process of constructing an matrix product state detailed in Section 5.2 brings the MPS in a *left-canonical* form. This implies that all the matrices are left-normalized, such that

$$\sum_{j_n} A^{j_n\dagger} A^{j_n} = I \ . \tag{75}$$

This is a consequence of the matrix U (from the SVD) fulfilling $U^\dagger U = I$. Since the matrices A^{j_n} are reshaped from U, these properties persists

$$\delta_{\alpha_n,\alpha'_n} = \sum_{\alpha_{n-1} j_n} (U^\dagger)_{\alpha_n,(\alpha_{n-1} j_n)} U_{(\alpha_{n-1} j_n),\alpha'_n}$$

$$= \sum_{\alpha_{n-1} j_n} (A^{j_n\dagger})_{\alpha_n,\alpha_{n-1}} A^{j_n}_{\alpha_{n-1},\alpha'_n}$$

$$= \sum_{j_n} \left(A^{j_n\dagger} A^{j_n} \right)_{\alpha_n.\alpha'_n}$$

Figure 10 illustrates a contraction of the bonds connecting two left-normalised matrices. As this
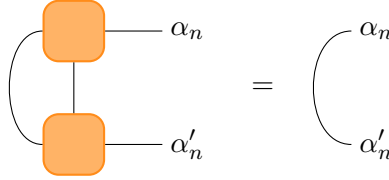
Figure 10: *Contraction over the left index (shown as the arc) and the physical index of two left-normalised matrices. The result is $\delta_{\alpha_n,\alpha'_n}$, adding the n'th site to the contraction of all previous sites to the left.*

contraction results in the identity per definition, one can contract left-normalised matrices without any explicit calculation. This is displayed diagrammatically through an arc, which is equivalent to an identity-tensor with two bond indices.

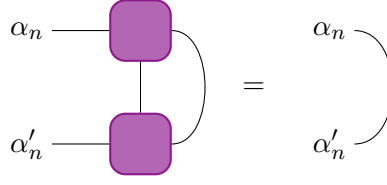**Right-canonical matrix product state**

One could also have built a a right-canonical MPS from eq. (68), had one started from other side of the chain. This implies multiplying U and S into the new Ψ-matrix, and reshaping $(V^\dagger)_{(\alpha_{n-1} j_n),\alpha_n}$ into matrices $B^{j_n}_{\alpha_{n-1},\alpha_n}$. Hence, the right-canonical form of the MPS of eq. (73) reads

$$|\psi\rangle = \sum_{j_1,...,j_N} B^{j_1} B^{j_2} \dots B^{j_{N-1}} B^{j_N} |j_1,\dots,j_N\rangle \ . \tag{76}$$

In this form all the matrices are right-normalized, whereby

$$\sum_{j_n} B^{j_n} B^{j_n\dagger} = I \ . \tag{77}$$

Note how right-normalised matrices are denoted by B^{j_n} opposed to left-normalised matrices, A^{j_n}. Figure 11 illustrates two right-normalised matrices contracted over their physical index.

Figure 11: *Contraction over the right index (shown as the arc) and the physical index of two right-normalised matrices.*

Mixed-canonical matrix product state

In practice one rarely finds use for a purely left- or right-canonical MPS. However, combining the two canonical forms listed above yields the mixed-canonical form. This form results in a natural bi-partitioning of the system into a Schmidt decomposition, and it is especially useful for measuring local properties of the state. CITE

Consider the procedure of building an MPS in the left-canonical form, where $c_{j_1 \ldots j_N}$ has been decomposed from the left up until site n

$$c_{j_1 \ldots j_N} = \sum_{\alpha_n} \left(A^{j_1} \ldots A^{j_n} \right)_{\alpha_n} S_{\alpha_n, \alpha_n} (V^\dagger)_{\alpha_n, (j_{n+1} \ldots j_N)} . \tag{78}$$

By reshaping $V^\dagger$ into the matrix $\Psi_{(\alpha_n j_{n+1} \ldots j_{N-1}), j_N}$, one can initiate a successive decomposition from the right, resulting in a set of right-normalized matrices. The final result reads

$$c_{j_1 \ldots j_N} = A^{j_1} \ldots A^{j_n} S B^{j_{n+1}} \ldots B^{j_N} , \tag{79}$$

which is illustrated in figure **??**. In this form the Schmidt decomposition can be read directly from the
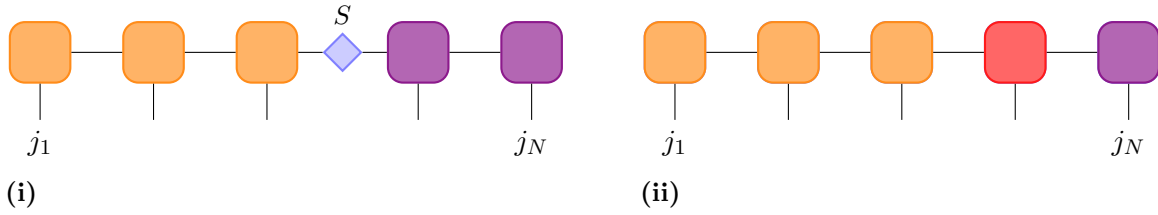
Figure 12: *Mixed-canonical form of an MPS. The form (i) directly brings the MPS into the form of a Schmidt decomposition, while the form (ii) is well suited for measuring local properties of the state.*

form of the MPS by introducing the vectors

$$|\alpha_n\rangle_A = \sum_{j_1, \ldots, j_n} \left(A^{j_1} \ldots A^{j_n} \right)_{1, \alpha_n} |j_1, \ldots, j_n\rangle \tag{80}$$

$$|\alpha_n\rangle_B = \sum_{j_{n+1}, \ldots, j_N} \left(B^{j_{n+1}} \ldots B^{j_N} \right)_{\alpha_n, 1} |j_{n+1}, \ldots, j_N\rangle , \tag{81}$$

whereby the state can be written in the form

$$|\psi\rangle = \sum_{\alpha_n} S_{\alpha_n, \alpha_n} |\alpha_n\rangle_A |\alpha_n\rangle_B . \tag{82}$$

In order for this to be a Schmidt decomposition $\sum_{\alpha_n} (S_{\alpha_n, \alpha_n})^2 = 1$, however this condition is fulfilled by default by the SVD. Furthermore, the states $|\alpha_n\rangle_A$ and $|\alpha_n\rangle_B$ have to be orthonormal respectively, which they are by construction.

Another useful version of the mixed-canonical form is depicted in figure 12ii, where the matrix S of eq. (79) has been multiplied unto the matrix either to the left or right of it. The result is a central cite, which does not follow any normalisation. This form is advantageous when measuring local properties of a state, as the overlap with itself simplifies to the multiplication of the matrices at the central cite.

Bringing a matrix product state into canonical form

Up until now all canonical forms were realised during the construction of the matrix product states. However, any arbitrary MPS can be be brought into a canonical form through a series of SVD's, again exploiting the unitarity or left-/right-normalization of the resulting matrices.

Consider a general MPS

$$|\psi\rangle = \sum_{j_1,\ldots,j_N} \sum_{\alpha_1,\ldots} M^{j_1}_{1,\alpha_1} M^{j_2}_{\alpha_1,\alpha_2} M^{j_3}_{\alpha_2,\alpha_3} \ldots |j_1,\ldots,j_N\rangle \ , \tag{83}$$

which has to be brought into a left-canonical form. By grouping the physical and left (row) index of $M^{j_1}_{1,\alpha_1}$, one can reshape the tensor into a single matrix, $M_{(j_1,1),\alpha_1}$. Applying an SVD yields $M = ASV^\dagger$, where $A^\dagger A = I$, such that A is left-normalized as desired. Thus, the left-normalisation of the first tensor of the MPS reads

$$
\begin{aligned}
|\psi\rangle &= \sum_{j_1,\ldots,j_N} \sum_{\alpha_1,\ldots} M_{(j_1,1),\alpha_1} M^{j_2}_{\alpha_1,\alpha_2} M^{j_3}_{\alpha_2,\alpha_3} \ldots |j_1,\ldots,j_N\rangle \\
&= \sum_{j_1,\ldots,j_N} \sum_{\alpha_1,\ldots} \sum_{s_1} A_{(j_1,1),s_1} S_{s_1,s_1} V^\dagger_{s_1,\alpha_1} M^{j_2}_{\alpha_1,\alpha_2} M^{j_3}_{\alpha_2,\alpha_3} \ldots |j_1,\ldots,j_N\rangle \\
&= \sum_{j_1,\ldots,j_N} \sum_{\alpha_1,\ldots} \sum_{s_1} A^{j_1}_{1,s_1} \left(S_{s_1,s_1} V^\dagger_{s_1,\alpha_1} M^{j_2}_{\alpha_1,\alpha_2} \right) M^{j_3}_{\alpha_2,\alpha_3} \ldots |j_1,\ldots,j_N\rangle \\
&= \sum_{j_1,\ldots,j_N} \sum_{\alpha_2,\ldots} \sum_{s_1} A^{j_1}_{1,s_1} \tilde{M}^{j_2}_{s_1,\alpha_2} M^{j_3}_{\alpha_2,\alpha_3} \ldots |j_1,\ldots,j_N\rangle \ , \tag{84}
\end{aligned}
$$

where $\tilde{M}^{j_2}_{s_1,\alpha_2} = \sum_{\alpha_1} S_{s_1,s_1} V^\dagger_{s_1,\alpha_1} M^{j_2}_{\alpha_1,\alpha_2}$. This procedure can be iterated through the entire chain, leaving the MPS in the left-canonical form [**?**].

Likewise, an MPS can be brought into a right-canonical form by grouping the physical index with the right (column) index of M yielding the SVD $M = USB$, where $BB^\dagger = I$. Thus, iterating through the chain from the right will produce a right-canonical MPS.

5.4 Overlaps and Efficient Contractions

Great reductions in computational cost can be achieved by contracting the tensor networks in the correct order. Consider the general case of two states $|\psi\rangle$ and $|\phi\rangle$ described by the matrices M and $\tilde{M}$. The overlap between these states reads

$$\langle\phi|\psi\rangle = \sum_{j_1,\ldots,j_N} \tilde{M}^{j_N\dagger} \ldots \tilde{M}^{j_1\dagger} M^{j_1} \ldots M^{j_N} \ , \tag{85}$$

which is represented diagrammatically in figure 13. The evaluation of the overlap can be drastically
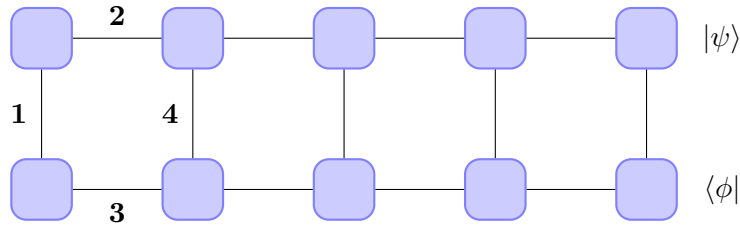
Figure 13: *Efficient contraction of the overlap between two general states $|\psi\rangle$ and $|\phi\rangle$. By contracting the bonds in the specified order the computational cost is greatly reduced.*

sped up by considering the optimal order of contractions, which corresponds to an optimal bracketing of eq. (85):

$$\langle\phi|\psi\rangle = \sum_{j_N} \tilde{M}^{j_N\dagger} \left(\ldots \left(\sum_{j_2} \tilde{M}^{j_2\dagger} \left(\sum_{j_1} \tilde{M}^{j_1\dagger} M^{j_1} \right) M^{j_2} \right) \ldots \right) M^{j_N} \ . \tag{86}$$

Within the innermost bracket a matrix is formed by multiplying a column and a row vector followed by the summation over the first physical index, j_1. In the remaining set of brackets three matrices are multiplied and the corresponding physical index is summed over. However, after the first contraction the complexity of the operation does not increase. Consider the worst case scenario of all the matrices being of dimension $(D \times D)$ with a local Hilbert space of dimension d. The total operational cost of the optimal contraction is $O(ND^3d)$ compared to otherwise exponential complexity of a random order of contractions [?]. The order of contractions described in eq. (86) is illustrated in figure 85.

When calculating a norm, $\langle \psi | \psi \rangle$, the canonical form of the MPS greatly reduces to computational time, as having an either left- or right-canonical MPS implies a norm of 1 without any contractions needed. In the case of a left-canonical for, every matrix product of eq. (86) is I due to left-orthogonality. Finally, summing over the final index simply yields 1.

5.5   Matrix Product Operators

A Matrix Product Operator (MPO) is an operator expressed in the formalism of an MPS. Thus, operators can easily be incorporated as part of the tensor networks, where they are evaluated by contraction over their bonds.

Consider a single coefficient of an MPS of the state ψ

$$\langle j_1, \ldots, j_N | \psi \rangle = \langle \boldsymbol{j} | \psi \rangle = M^{j_1} M^{j_2} \ldots M^{j_N} . \tag{87}$$

Expressing an operator $\hat{O}$ in the basis of the local states, one can write it in a similar manner

$$\hat{O} = \sum_{\boldsymbol{j}, \boldsymbol{j}'} | \boldsymbol{j} \rangle \langle \boldsymbol{j} | \hat{O} | \boldsymbol{j}' \rangle \langle \boldsymbol{j}' | = \sum_{\boldsymbol{j}, \boldsymbol{j}'} W^{j_1, j_1'} W^{j_2, j_2'} \ldots W^{j_N, j_N'} | \boldsymbol{j} \rangle \langle \boldsymbol{j}' | , \tag{88}$$

where the coefficients are $\langle \boldsymbol{j} | \hat{O} | \boldsymbol{j}' \rangle = W^{j_1, j_1'} W^{j_2, j_2'} \ldots W^{j_N, j_N'}$. The matrices $W^{j_n, j_n'}$ are just like the M-matrices, except the the representation of the operators needs both an ingoing and an outgoing physical index. This corresponds graphically to having two vertical lines; one corresponding to the ingoing physical state, the other corresponding to the outgoing physical state. A pictorial representation of the operator $\hat{O}$ can be seen in figure 14.
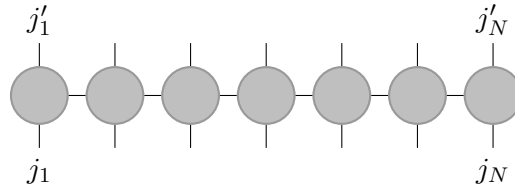

Figure 14: *An operator $\hat{O}$ expressed in the MPS form (MPO). The resulting matrix product has two vertical lines corresponding to an ingoing and outgoing physical state.*

Applying an MPO to an MPS

Applying a matrix product operator to a matrix product state is simply a matrix multiplication, where the matching physical indices are summed over:

$$
\begin{aligned}
\hat{O}\left|\psi\right\rangle &= \sum_{\boldsymbol{j},\boldsymbol{j'}} \left(M^{j_1'} M^{j_2'} \dots \right) \left(W^{j_1',j_1} W^{j_2',j_2} \dots \right) \left|\boldsymbol{j}\right\rangle \\
&= \sum_{\boldsymbol{j},\boldsymbol{j'}} \sum_{\boldsymbol{\alpha},\boldsymbol{\beta}} \left(M^{j_1'}_{1,\alpha_1} M^{j_2'}_{\alpha_1,\alpha_2} \dots \right) \left(W^{j_1',j_1}_{1,\beta_1} W^{j_2',j_2}_{\beta_1,\beta_2} \dots \right) \left|\boldsymbol{j}\right\rangle \\
&= \sum_{\boldsymbol{j},\boldsymbol{j'}} \sum_{\boldsymbol{\alpha},\boldsymbol{\beta}} \left(M^{j_1'}_{1,\alpha_1} W^{j_1',j_1}_{1,\beta_1} \right) \left(M^{j_2'}_{\alpha_1,\alpha_2} W^{j_2',j_2}_{\beta_1,\beta_2} \right) \cdots \left|\boldsymbol{j}\right\rangle \\
&= \sum_{\boldsymbol{j}} \sum_{\boldsymbol{\alpha},\boldsymbol{\beta}} N^{j_1}_{(1,1),(\alpha_1,\beta_1)} N^{j_2}_{(\alpha_1,\beta_1),(\alpha_2,\beta_2)} \cdots \left|\boldsymbol{j}\right\rangle \\
&= \sum_{\boldsymbol{j}} N^{j_1} N^{j_2} \dots \left|\boldsymbol{j}\right\rangle \;=\; \left|\phi\right\rangle
\end{aligned}
\tag{89}
$$

The result is a new MPS, $\left|\phi\right\rangle$, which is described by the matrices N^{j_n} and is illustrated in figure 15. These matrices have the dimensions of the product of the dimensions of the original MPS and MPO. Thus, applying an operator leaves the form of the MPS invariant at a cost of increased matrix dimensions. If the dimension of the MPS is D, while the dimension of the MPO is D_W, the total
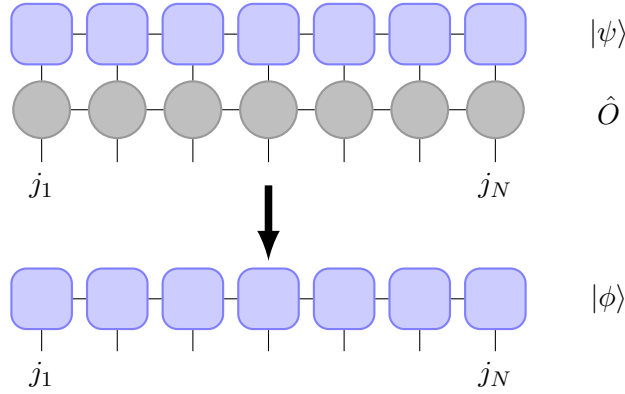
Figure 15: *Application of an MPO, $\hat{O}$, on an MPS, $\left|\psi\right\rangle$. Matching physical indices are contracted resulting in a new MPS, $\left|\phi\right\rangle$, with increased matrix dimensions.*

computational cost of the operation is $O(N d^2 D_W^2 D^2)$.[**?**, 25]

5.6 Correlation Functions and Measurement of Local Properties

Measuring local properties of a state is achieved by calculating the expectation value of local operators. Consider the local operator $\hat{O}^{[n]}$, where the square brackets denote the site, on which the $\hat{O}$ operates. As $\hat{O}^{[n]}$ is only acts on site n, it can be expressed in the basis of said site

$$
\hat{O}^{[n]} = \sum_{j_n, j_n'} O^{j_n, j_n'} \left|j_n\right\rangle \left\langle j_n'\right| \; .
\tag{90}
$$

Applying a local operator to a state implies applying the identity operator on all other sites. The resulting operator, $\hat{O} = \hat{I}^{[1]} \otimes \hat{I}^{[2]} \otimes \dots \otimes \hat{O}^{[n]} \otimes \dots \otimes \hat{I}^{[N]}$, can then be expressed as an MPO and readily be applied to a matrix product state. However, the calculation is greatly simplified when considering an MPS in a mixed-canonical form, where all matrices left of site n are left-normalized, while all matrices to the right are right-normalized. In this case, the entire tensor network on either side of site n can be contracted without any calculation. The remaining network needed to be contracted is

shown in figure 16i, which is simply the sum

$$\langle\psi|\,\hat{O}^{[n]}\,|\psi\rangle = \sum_{j_n,j'_n} O^{j_n,j'_n}\,\mathrm{Tr}\left(M^{j_n\dagger}M^{j'_n}\right) \tag{91}$$

with the computational cost $O(D^2 d^2)$ [?]. Very similar is the case of multiple-site local operator.

(i)   (ii)
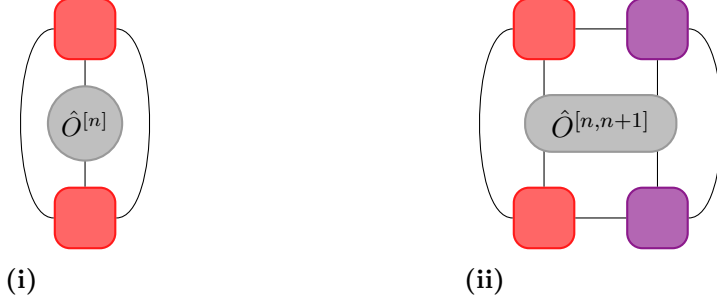
Figure 16: *Measurement of local properties of a matrix product state in the mixed-canonical form.*

However, sites on which the operator act can not be contracted explicitly. Thus, the resulting tensor network will look like the example shown in figure 16ii, where a two-site operator is measured.

Also correlation functions are calculated efficiently using matrix product states in the mixed-canonical form. Consider the correlation $\langle\psi|\,\hat{O}^{[n]}\hat{Q}^{[n+k]}\,|\psi\rangle$, whose corresponding tensor network is shown in figure 17. Again, having brought the MPS unto a mixed-canonical form results in the outer
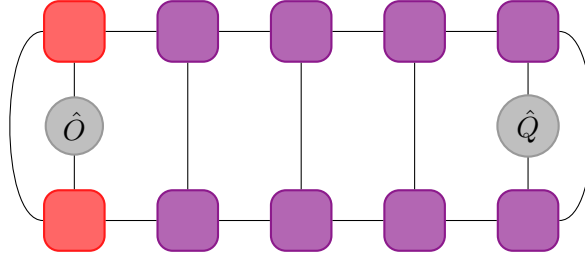
Figure 17: *Tensor network for the correlation function $\langle\psi|\,\hat{O}^{[n]}\hat{Q}^{[n+4]}\,|\psi\rangle$. The outer parts of the network are implicitly contracted to identities following the mixed-canonical form of the MPS.*

parts of the network being explicitly contracted as identities. However, the otherwise right-normalised tensors between the two operators can not be contracted as identities, as the right-most operator breaks the canonical form. Thus, one has to contract a network of length $k+1$, which is done most efficiently following the optimal bracketing described in eq. (89). The complexity of the entire contraction is of order $O(kD^3 d)$.

Correlation length

Although the MPS formalism excels at describing one dimensional systems, it struggles with describing long ranged correlations, due to how it is constructed. Consider a general MPS in no particular canonical form, as described in eq. (83). The *transfer operator* is defined as

$$\hat{E}^{[n]} = \sum_{\alpha_{n-1},\alpha'_{n-1}}\sum_{\alpha_n,\alpha'_n}\left(\sum_{j_n}M^{[n]j_n*}\otimes M^{[n]j_n}\right)_{(\alpha_{n-1}\alpha'_{n-1}),(\alpha_n\alpha'_n)}\left(|\alpha_{n-1}\rangle\,\langle\alpha'_{n-1}|\right)\left(|\alpha_n\rangle\,\langle\alpha'_n|\right), \tag{92}$$

where the expression in the brackets is the matrix elements of the operator, and α_n are the physical indices of the matrices. The transfer operator is essentially a complete, positive map from operators defined on a block of the lattice of length $n-1$ to a block of length n, such that

$$\{|\alpha_{n-1}\rangle\,\langle\alpha'_{n-1}|\} \rightarrow \{|\alpha_n\rangle\,\langle\alpha'_n|\}\,. \tag{93}$$

One important property of the transfer operator, or transfer matrix, is that all eigenvalues $|\lambda_k| \leq 1$ [32].

Generalizing the transfer operator to contraction with an operator $\hat{O}$ gives

$$E_O^{[n]} = \sum_{j_n, j_n'} O^{j_n, j_n'} M^{[n]j_n*} \otimes M^{[n]j_n'} . \tag{94}$$

Using this one can write the correlation function of two general operators on sites i and j as

$$\begin{aligned}
\langle\psi| \hat{O}^{[i]}\hat{O}^{[j]} |\psi\rangle &= \operatorname{Tr} E^{[1]} \ldots E^{[i-1]} E_O^{[i]} E^{[i+1]} \ldots E^{[j-1]} E_O^{[j]} E^{[j+1]} \ldots E^{[N]} \\
&= \operatorname{Tr} E_O^{[i]} E^{[j-i-1]} E_O^{[j]} E^{[L-j+i-1]} \\
&= \sum_{l,k} \langle l| E_O^{[i]} |k\rangle \lambda_k^{j-i-1} \langle k| E_O^{[j]} |l\rangle \lambda_l^{N-j+i-1} \\
&= \sum_k \langle 1| E_O^{[i]} |k\rangle \lambda_k^{j-i-1} \langle k| E_O^{[j]} |1\rangle \qquad (\text{for} N \to \infty)
\end{aligned} \tag{95}$$

where λ is the eigenvalues of the transfer matrix. Since $|\lambda_k| \leq 1$, only the leading eigenvalue $\lambda_1 = 1$ remains as $N \to \infty$. Defining the distance between two sites as $r = |j - i - 1|$ and the correlation decay, or correlation length, as $\xi_k = -1/\ln \lambda_k$, the correlation function can be written as

$$\frac{\langle\psi| \hat{O}^{[i]}\hat{O}^{[j]} |\psi\rangle}{\langle\psi|\psi\rangle} = c_1 + \sum_{k=2} c_k e^{-r/\xi_k} , \tag{96}$$

where $c_k = \langle 1| E_O^{[i]} |k\rangle \langle k| E_O^{[j]} |1\rangle$. [32]

Equation (96) shows that the correlation function is a linear combination of exponential functions. Since this was derived without any assumptions regarding neither the MPS nor the operators, this results can be considered general. Thus, any finite-dimensional MPS will only be able to approximate the true correlation of a system.

This is the cause of the difficulty of describing the long range correlations, such as the Superfluid single-particle correlations. While single-particle correlations decay exponentially for the Mott-Insulator, it decays following a power-law for Superfluids

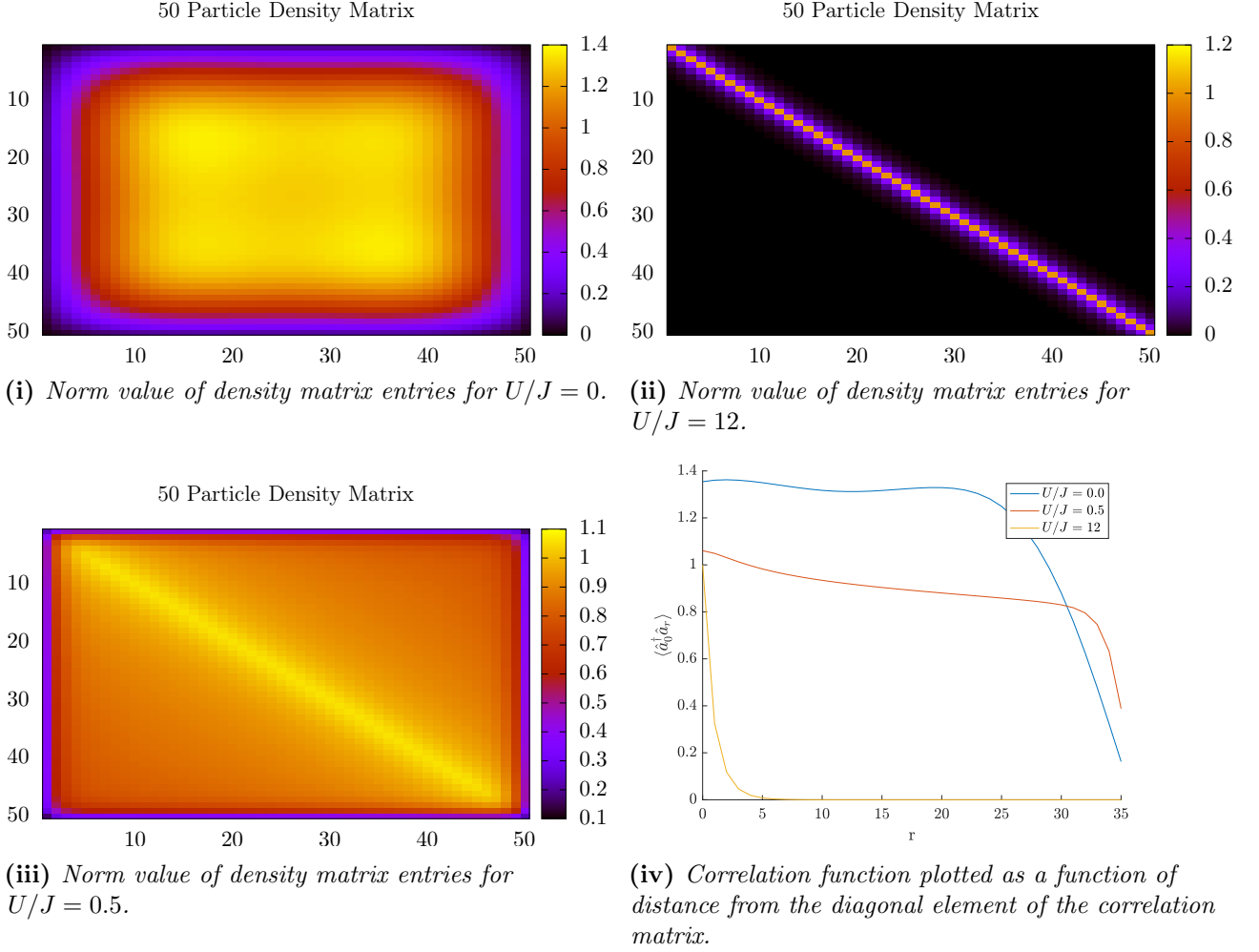$$\langle \hat{a}_i^\dagger \hat{a}_j \rangle \sim |i - j|^{-K_b/2} , \tag{97}$$

where K_b is the Tomonaga-Luttinger parameter [8]. For short distances equation (96) is able to accurately approximate a power-law, however, as distances grow larger, only the slowest exponential decay will survive. Hence, the correlation turns into a pure exponential decay with $\xi = -1/\ln \lambda$, where λ is the largest eigenvalue of $\hat{E}$ contributing to the correlation.

Visualization of density matrices

One way of displaying the correlations of the system is to plot its density matrix, whose entries are given by

$$\rho_{i,j} = \langle\psi| \hat{a}_i^\dagger \hat{a}_j |\psi\rangle . \tag{98}$$

Figures 18i and 18ii show the density matrix of the 50 particle system plotted for the Superfluid and the Mott-Insulator limit respectively. In the SF limit long-range correlations are present, which is seen by large off-diagonal elements. However, as discussed previously, in the MPS approximation all correlations decay exponentially, which causes issues when trying to approximate the very long range correlations of the system. This is visualized in figure 18iv where the correlation function is plotted against distance from the diagonal. The Superfluid graph has a hump on it, which is an artefact of the DMRG algorithm. Due to the very long correlation length the graph should be almost flat except for the rapid drop in the end, which is due to the open boundary conditions. The graph in figure 18iv is the result of the DMRG algorithm attempting to express this long range correlation as a series of exponentials.

50 Particle Density Matrix

(i) *Norm value of density matrix entries for* $U/J = 0$.

50 Particle Density Matrix

(ii) *Norm value of density matrix entries for* $U/J = 12$.

50 Particle Density Matrix

(iii) *Norm value of density matrix entries for* $U/J = 0.5$.

(iv) *Correlation function plotted as a function of distance from the diagonal element of the correlation matrix.*

In the MI limit no interaction takes place between sites and the correlation length is zero, leading to a correlation matrix consisting only of diagonal elements of equal magnitude. Figure (124) shows some off-diagonal elements of non-zero magnitude, however, this system is not a pure Mott-Insulator, as $U/J = 12$. Nevertheless, the correlations are well described by only a single exponential function, as shown in figure 18iv.

Finally, figure 18iii illustrates the density matrix for a system with $U/J = 0.5$, which is primarily as Superfluid, although, as seen in the figure, has a well defined diagonal. Inspecting its correlation function reveals that the best approximation is by a power-law, thus confirming that the system is indeed a Superfluid.

6 Calculating Ground States with MPS

For large systems exact diagonalization of the Hamiltonian is impossible, whereby one must resort to variational methods in order to find ground states. This involves finding the MPS, $|\psi\rangle$, which minimizes

$$E = \frac{\langle\psi|\hat{H}|\psi\rangle}{\langle\psi|\psi\rangle} \ . \tag{99}$$

The most efficient way to do this, is to express the Hamiltonian as an MPO as described in eq. (88), whereby it easily can be applied to an MPS. While this may seem difficult at first, it can actually be done without any lengthy calculations. An example is given in Appendix B, where the Bose-Hubbard Hamiltonian is formulated as tensors.

6.1 Efficient Application of a Hamiltonian to an MPS

In section 5.5 it was explained how to apply an MPO to an MPS, and it was shown how to efficiently evaluate local operators. However, since $\hat{H}\ket{\psi}$ must be evaluated many times during variational methods, one must find even more efficient way of applying the operator.

Consider an MPS in a mixed-canonical form

$$
\begin{aligned}
\ket{\psi} &= \sum_{\boldsymbol{j}} A^{j_1}\dots A^{j_{n-1}}\Psi^{j_n}B^{j_{n+1}}\dots B^{j_N}\ket{\boldsymbol{j}} \\
&= \sum_{\alpha_{n-1},\alpha_n}\ket{\alpha_{n-1}}_A \Psi^{j_n}_{\alpha_{n-1},\alpha_n}\ket{\alpha_n}_B \ ,
\end{aligned}
\tag{100}
$$

where Ψ^{j_n} is the central site, and $\ket{\alpha_{n-1}}_A$ and $\ket{\alpha_n}_B$ are block states introduced in eq. (80) and (81) respectively. Huge reductions in computational cost of the variational search can be found by re-using as many calculations as possible. In the basis $\{\ket{\alpha_{n-1}}\ ,\ \ket{j_n}\ ,\ \ket{\alpha_n}\}$ the individual matrix elements of the Hamiltonian can be expressed as

$$
\bra{\alpha_{n-1}j_n\alpha_n}\hat{H}\ket{\alpha'_{n-1}j'_n\alpha'_n} = \sum_{\boldsymbol{j},\boldsymbol{j'}} W^{j_1,j'_1}\dots W^{j_N,j'_N}\braket{\alpha_{n-1}j_n\alpha_n|\boldsymbol{j}}\braket{\boldsymbol{j'}|\alpha'_{n-1}j'_n\alpha'_n} \ .
$$

Since the basis of local states $\{\ket{\boldsymbol{j}}\}$ shares a state with the basis $\{\ket{\alpha_{n-1}}\ ,\ \ket{j_n}\ ,\ \ket{\alpha_n}\}$, the above expression can be re-written using $\sum_{\boldsymbol{j}}\braket{j_n|\boldsymbol{j}} = \sum_{\boldsymbol{j*}}\ket{\boldsymbol{j*}}$, where "$*$" means "excluding j_n". Thus,

$$
\begin{aligned}
&\bra{\alpha_{n-1}j_n\alpha_n}\hat{H}\ket{\alpha'_{n-1}j'_n\alpha'_n} = \\
&= \sum_{\boldsymbol{j*},\boldsymbol{j'*}} W^{j_1,j'_1}\dots W^{j_n,j'_n}\dots W^{j_N,j'_N} \\
&\qquad \times \braket{\alpha_{n-1}|j_1\dots j_{n-1}}\braket{\alpha_n|j_{n+1}\dots j_N}\braket{j'_1\dots j'_{n-1}|\alpha'_{n-1}}\braket{j'_{n+1}\dots j'_N|\alpha'_n} \\
&= \sum_{\boldsymbol{j*},\boldsymbol{j'*}} W^{j_1,j'_1}\dots W^{j_n,j'_n}\dots W^{j_N,j'_N} \\
&\qquad \times \left(A^{j_1}\dots A^{j_{n-1}}\right)^*_{1,\alpha_{n-1}}\left(B^{j_{n+1}}\dots B^{j_N}\right)^*_{\alpha_n,1}\left(A^{j'_1}\dots A^{j'_{n-1}}\right)_{1,\alpha'_{n-1}}\left(B^{j'_{n+1}}\dots B^{j'_N}\right)_{\alpha'_n,1} \\
&= \sum_{\alpha_n,\beta_n,\alpha'_n}\left(\sum_{j_1,j'_1}A^{j_1*}_{1,\alpha_1}W^{j_1,j'_1}_{1,\beta_1}A^{j'_1}_{1,\alpha'_1}\right)\left(\sum_{j_2,j'_2}A^{j_2*}_{\alpha_1,\alpha_2}W^{j_2,j'_2}_{\beta_1,\beta_2}A^{j'_2}_{\alpha'_1,\alpha'_2}\right)\dots W^{j_n,j'_n}_{\beta_{n_1},\beta_n} \\
&\qquad \times \left(\sum_{j_{n+1},j'_{n+1}}B^{j_{n+1}*}_{\alpha_n,\alpha_{n+1}}W^{j_{n+1},j'_{n+1}}_{\beta_n,\beta_{n+1}}B^{j'_{n+1}}_{\alpha'_n,\alpha'_{n+1}}\right)\left(\sum_{j_N,j'_N}B^{j_N*}_{\alpha_{N-1},1}W^{j_N,j'_N}_{\beta_{N-1},1}B^{j'_N}_{\alpha'_{N-1},1}\right) \ .
\end{aligned}
\tag{101}
$$

While this expression may seem terrible complicated due to all the indices, it is actually rather easy to understand. First, the matrix element is written excluding the local basis state $\ket{j_n}$. Next, the Hamilton MPO is projected into the block states of A, $\ket{\alpha_{n-1}}_A$, and B, $\ket{\alpha_n}_B$. Finally, the matrices are grouped according to their expansion in the local basis. Working with the above expression appears cumbersome, but it is merely a decoupling of the system into three distinct parts, which can be seen in figure 19. Since both the left and right side of the network is connected, one can contract these parts into two separate tensors L and R called "environments":

$$
L_{\alpha_{n-1},\beta_{n-1},\alpha'_{n-1}} = \sum_{\substack{\{\alpha_i\beta_i\alpha'_i\}\\i<n-1}}\left(\sum_{j_1,j'_1}A^{j_1*}_{1,\alpha_1}W^{j_1,j'_1}_{1,\beta_1}A^{j'_1}_{1,\alpha'_1}\right)\dots\left(\sum_{j_{n-1},j'_{n-1}}A^{j_{n-1}*}_{\alpha_{n-2},\alpha_{n-1}}W^{j_{n-1},j'_{n-1}}_{\beta_{n-2},\beta_{n-1}}A^{j'_{n-1}}_{\alpha'_{n-2},\alpha'_{n-1}}\right)
\tag{102}
$$

$$
R_{\alpha_n,\beta_n,\alpha'_n} = \sum_{\substack{\{\alpha_i\beta_i\alpha'_i\}\\i>n}}\left(\sum_{j_{n+1},j'_{n+1}}B^{j_{n+1}*}_{\alpha_n,\alpha_{n+1}}W^{j_{n+1},j'_{n+1}}_{\beta_n,\beta_{n+1}}B^{j'_{n+1}}_{\alpha'_n,\alpha'_{n+1}}\right)\left(\sum_{j_N,j'_N}B^{j_N*}_{\alpha_{N-1},1}W^{j_N,j'_N}_{\beta_{N-1},1}B^{j'_N}_{\alpha'_{N-1},1}\right)
\tag{103}
$$

Figure 19: *Representation of the matrix element $\langle \alpha_{n-1} j_n \alpha_n | \hat{H} | \alpha'_{n-1} j'_n \alpha'_n \rangle$ as an tensor network. Expressing the matrix element in this form decouples the network in three parts: The matrices of the MPO, $W^{[n]}$, connecting the physical sites of the matrix element, and contracted parts L and R consisting of the rest of the MPO and the left- and right-normalised part of the MPS respectively.*

From these contractions, the obvious tripartite structure of the Hamiltonian matrix element, as seen in figure 19, can be written in a compact way

$$\langle \alpha_{n-1} j_n \alpha_n | \hat{H} | \alpha'_{n-1} j'_n \alpha'_n \rangle = \sum_{\beta_{n-1}, \beta_n} L_{\alpha_{n-1}, \beta_{n-1}, \alpha'_{n-1}} W^{j_n, j'_n}_{\beta_{n_1}, \beta_n} R_{\alpha_n, \beta_n, \alpha'_n} . \tag{104}$$

Finally, applying this parametrization of the Hamiltonian to the MPS of eq. (100) yields [32]

$$\hat{H} |\psi\rangle = \sum_{\beta_{n-1}, \beta_n} \sum_{\alpha'_{n-1}, j'_n, \alpha'_n} L_{\alpha_{n-1}, \beta_{n-1}, \alpha'_{n-1}} W^{j_n, j'_n}_{\beta_{n_1}, \beta_n} R_{\alpha_n, \beta_n, \alpha'_n} \Psi^{j'_n}_{\alpha'_{n-1}, \alpha'_n} |\alpha_{n-1}\rangle_A |j_n\rangle |\alpha_n\rangle_B . \tag{105}$$

As mentioned earlier, evaluating $\hat{H} |\psi\rangle$ must be done many times during a variational search of the ground state, hence this operation must be executed as fast as possible. Examining eq. (105) one will notice, that while the boundaries of L and R will change depending on which site is being optimized, the bulk of the two tensors remain constant through a lot of the calculations. Instead of calculating L and R from eq. (102) and (103) for every evaluation of eq. (105), one can iteratively build them, since they only change by one column of the network at a time. Thus, a large number of computations can be reused.

Consider the construction of the tensor $L^{[i]}$. This can be built iteratively from the left by contracting the previous left-tensor $L^{[i-1]}$ with the i'th column of the network consisting of $A^{[i]}$, $W^{[i]}$ and $A^{[i]\dagger}$

$$L^{[i]}_{\alpha_i, \beta_i, \alpha'_i} = \sum_{\substack{j_i, j'_i \\ \alpha_{i-1}, \beta_{i-1}, \alpha'_{i-1}}} W^{[i] j_i, j'_i}_{\beta_{i-1}, \beta_i} \left(A^{[i] j_i \dagger} \right)_{\alpha_i, \alpha_{i-1}} L^{[i-1]}_{\alpha_{i-1}, \beta_{i-1}, \alpha'_{i-1}} A^{[i] j'_i}_{\alpha'_{i-1}, \alpha'_i} . \tag{106}$$

This iterative update of $L^{[i]}$ can be seen illustrated in figure 20. The square-bracket notation has been re-introduced to keep track of the tensors relation to the physical sites. In order to remain consistent with notation, the dummy scalars $L^{[0]}_{\alpha_0, \beta_0, \alpha'_0} = 1 = \alpha_0, \beta_0, \alpha'_0$ has been introduced.

It is important to store every iteration of $L^{[i]}$, since L will grow and shrink constantly throughout the variational search of the ground state, whereby every iteration of $L^{[i]}$ will be used multiple times. The same applies when building the right environment, R. Here one starts from the right and moves left when iteratively contracting the tensor. By applying optimal bracketing, the computational cost of updating the environments scales as $O(dD^3 D_W)$.

6.2 Iterative Ground State Search and the DMRG Algorithm

In order to find the ground state of the system on can introduce a Lagrangian multiplier, λ, and extremize

$$\langle \psi | \hat{H} |\psi\rangle - \lambda \langle \psi | \psi \rangle , \tag{107}$$
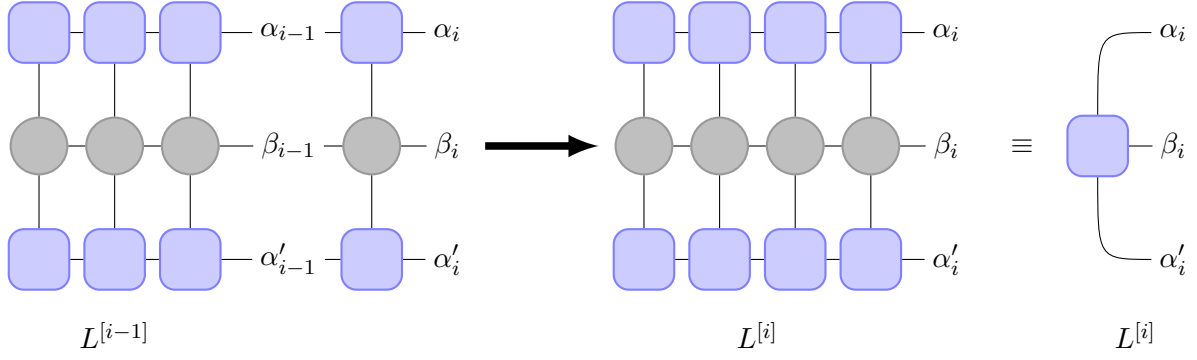
Figure 20: *Iterative update from $L^{[i-1]}$ to $L^{[i]}$. This is done through a contraction of $L^{[i-1]}$ with $A^{[i]}$, $W^{[i]}$ and $A^{[i]\dagger}$. The result is a tensor with three horizontal legs.*

whereby the desired ground state, $|\psi\rangle$, and ground state energy, λ^0, will be reached.

Trying to optimize an entire MPS at once is a highly non-linear problem involving an extremely large number of variables. However, the problem can be linearised by only considering the variables of a single tensor (site) at a time, while keeping the rest of the MPS constant. By varying just a single tensor at a time, one will continuously find states lower in energy, until convergence is reached. However, this procedure is very prone to getting stuck in a local extrema. To circumvent this, one can consider two sites at a time and optimize with regards to a two-site tensor, created by momentarily merging the two sites [41].

Consider the variation of the tensors $M^{[n]}$ and $M^{[n+1]}$. Expressing the minimization problem of eq. (107) in terms of the left and right environments (as done in eq. (105)) yields

$$
\langle\psi|\hat{H}|\psi\rangle = \sum_{\substack{j_n,j_n' \\ j_{n+1},j_{n+1}'}} \sum_{\alpha_{n-1}',\alpha_n',\alpha_{n+1}'} \sum_{\alpha_{n-1},\alpha_n,\alpha_{n+1}} \sum_{\beta_{n-1},\beta_n,\beta_{n+1}} L^{[n-1]}_{\alpha_{n-1},\beta_{n-1},\alpha_{n-1}'} W^{[n]j_n,j_n'}_{\beta_{n_1},\beta_n} W^{[n+1]j_{n+1},j_{n+1}'}_{\beta_n,\beta_{n+1}}
$$
$$
\times R^{[n+2]}_{\alpha_{n+1},\beta_{n+1},\alpha_{n+1}'} M^{[n]j_n}_{\alpha_{n-1},\alpha_n} M^{[n]j_n'*}_{\alpha_{n-1}',\alpha_n'} M^{[n+1]j_{n+1}}_{\alpha_n,\alpha_{n+1}} M^{[n+1]j_{n+1}'*}_{\alpha_n',\alpha_{n+1}'} \tag{108}
$$
$$
\langle\psi|\psi\rangle = \sum_{j_n,j_{n+1}} \sum_{\substack{\alpha_{n-1}' \\ \alpha_n',\alpha_{n+1}'}} \sum_{\substack{\alpha_{n-1},\alpha_n \\ \alpha_{n+1}}} \Psi^A_{\alpha_{n-1},\alpha_{n-1}'} M^{[n]j_n}_{\alpha_{n-1},\alpha_n} M^{[n]j_n'*}_{\alpha_{n-1}',\alpha_n'} M^{[n+1]j_{n+1}}_{\alpha_n,\alpha_{n+1}} M^{[n+1]j_{n+1}'*}_{\alpha_n',\alpha_{n+1}'} \Psi^B_{\alpha_{n+1},\alpha_{n+1}'},
$$
$$
\tag{109}
$$

where the Hamiltonian from eq. (105) has been re-ordered to accommodate examining two sites, n and $n+1$, at a time, and

$$
\Psi^A_{\alpha_{n-1},\alpha_{n-1}'} = \sum_{j_1,\dots,j_{n-1}} \left(M^{j_{n-1}\dagger}\dots M^{j_1\dagger}M^{j_1}\dots M^{j_{n-1}} \right)_{\alpha_{n-1},\alpha_{n-1}'} \tag{110}
$$
$$
\Psi^B_{\alpha_{n+1},\alpha_{n+1}'} = \sum_{j_{n+2},\dots,j_N} \left(M^{j_{n+2}}\dots M^{j_N} M^{j_N\dagger}\dots M^{j_{n+2}\dagger} \right)_{\alpha_{n+1}',\alpha_{n+1}}. \tag{111}
$$

Further simplifications can be made for mixed-canonical forms, if sites 1 through $n-1$ are left-normalized, and sites $n+2$ through N are right-normalized, whereby

$$
\Psi^A_{\alpha_{n-1},\alpha_{n-1}'} = \delta_{\alpha_{n-1},\alpha_{n-1}'} \quad , \quad \Psi^B_{\alpha_{n+1},\alpha_{n+1}'} = \delta_{\alpha_{n+1},\alpha_{n+1}'}. \tag{112}
$$

Finding the extremum of eq. (107) with respect to $M^{[n]j_n'*}_{\alpha_{n-1}',\alpha_n'}$ $M^{[n+1]j_{n+1}'*}_{\alpha_n',\alpha_{n+1}'}$ is done through the following sequence:

Two-site update for iterative ground state search

1. **Merge:** Contract the two matrices $M^{[n]}$ and $M^{[n+1]}$ over the bond α_n creating a two-site tensor

$$
\Theta^{j_n,j_{n+1}}_{\alpha_{n-1},\alpha_{n+1}} = \sum_{\alpha_n} M^{[n]j_n}_{\alpha_{n-1},\alpha_n} M^{[n+1]j_{n+1}}_{\alpha_n,\alpha_{n+1}} \tag{113}
$$

2. **Solve eigenproblem:** This yields an eigenvalue problem, which can be seen by reshaping

$$H_{(\alpha_{n-1}j_nj_{n+1},\alpha_{n+1}),(\alpha'_{n-1}j'_nj'_{n+1},\alpha'_{n+1})} =$$
$$= \sum_{\substack{\beta_{n-1},\beta_n \\ \beta_{n+1}}} L^{[n-1]}_{\alpha_{n-1},\beta_{n-1},\alpha'_{n-1}} \, W^{[n]j_n,j'_n}_{\beta_{n_1},\beta_n} \, W^{[n+1]j_{n+1},j'_{n+1}}_{\beta_n,\beta_{n+1}} \, R^{[n+2]}_{\alpha_{n+1},\beta_{n+1},\alpha'_{n+1}} \tag{114}$$

$$v_{\alpha_{n-1}j_nj_{n+1}\alpha_{n+1}} = \Theta^{j_n,j_{n+1}}_{\alpha_{n-1},\alpha_{n+1}} \tag{115}$$

such that

$$Hv - \lambda v = 0 \ . \tag{116}$$

Solving this for the lowest eigenvalue λ_0 yields $v^0_{\alpha_{n-1}j_nj_{n+1}\alpha_{n+1}}$, which can be reshaped back to the now optimized two-site tensor, $\tilde{\Theta}^{j_n,j_{n+1}}_{\alpha_{n-1},\alpha_{n+1}}$.

3. **Unmerge:** Reshape the updated $\tilde{\Theta}^{j_n,j_{n+1}}_{\alpha_{n-1},\alpha_{n+1}}$ to a matrix and perform an SVD yielding

$$\tilde{\Theta}_{(j_n\alpha_{n-1}),(j_{n+1}\alpha_{n+1})} = \sum_{\alpha_n} U^{j_n}_{\alpha_{n-1},\alpha_n} S_{\alpha_n,\alpha_n} (V^\dagger)^{j_{n+1}}_{\alpha_n,\alpha_{n+1}} \ . \tag{117}$$

This causes the bond dimension to increase $D \to dD$, which must be truncated by keeping only the D largest singular values of S.

4. **Update environments:** The last step depends on which direction, one is iterating trough the chain. Here, the left- and right-normalization of U and $V^\dagger$ is used to update the environments. *Going right*: Update the left environment

$$\tilde{L}^{[n]}_{\alpha_n,\beta_n,\alpha'_n} = \sum_{\substack{j_n,j'_n \\ \alpha_{n-1},\beta_{n-1},\alpha'_{n-1}}} L^{[n-1]}_{\alpha_{n-1},\beta_{n-1},\alpha'_{n-1}} \, U^{j_n}_{\alpha_{n-1},\alpha_n} \, W^{[n]j_n,j'_n}_{\beta_{n-1},\beta_n} \, U^{j'_n*}_{\alpha'_{n-1},\alpha'_n} \ , \tag{118}$$

and build the matrix of the right site

$$\tilde{M}^{[n+1]j_{n+1}}_{\alpha_n,\alpha_{n+1}} = \sum_{\alpha_n} S_{\alpha_n,\alpha_n} (V^\dagger)^{j_{n+1}}_{\alpha_n,\alpha_{n+1}} \ . \tag{119}$$

Going left: Update the right environment

$$\tilde{R}^{[n+1]}_{\alpha_n,\beta_n,\alpha'_n} = \sum_{\substack{j_{n+1},j'_{n+1} \\ \alpha_{n+1},\beta_{n+1},\alpha'_{n+1}}} R^{[n+2]}_{\alpha_{n+1},\beta_{n+1},\alpha'_{n+1}} \left(V^\dagger\right)^{j_{n+1}}_{\alpha_n,\alpha_{n+1}} \, W^{[n+1]j_{n+1},j'_{n+1}}_{\beta_n,\beta_{n+1}} \, \left(V^\dagger\right)^{j_{n+1}*}_{\alpha_n,\alpha_{n+1}} \ , \tag{120}$$

and build the matrix of the left site

$$\tilde{M}^{[n]j_n}_{\alpha_{n-1},\alpha_n} = \sum_{\alpha_n} U^{j_n}_{\alpha_{n-1},\alpha_n} S_{\alpha_n,\alpha_n} \ . \tag{121}$$

This concludes the two-site update sequence, which is illustrated in figure 21. After performing the sequence, one can move *one site* to either left or right, depending on which direction, one is iterating.

Some comments regarding this sequence are in order: The matrices of the eigenvalue problem have dimensions $(d^2D^2 \times d^2D^2)$, which is generally too much for exact diagonalization, however, since only the lowest eigenvalue is of interest, one can use an iterative eigensolver. CITE Furthermore, if the MPS is not in the proper mixed-canonical form, the eigenvalue problem turns into a generalized eigenvalue problem, which can be numerically quite demanding. Thus, updating the left and right environments in step (4) is necessary, since it leads to great simplifications in step (2). Lastly, one could also consider just a single site when updating, however, this method is very prone to getting stuck [42]. By updating two sites at once, one actually optimizes the bond between them. Hence, after updating the two sites, one must only iterate a single site. Optimization is done with regards to the current configuration, whereby it depends on previous updates. To compensate for this, one must sweep through the entire system multiple times, which leads to the following algorithm for iterative ground state search, which follows the structure of the DMRG algorithm:
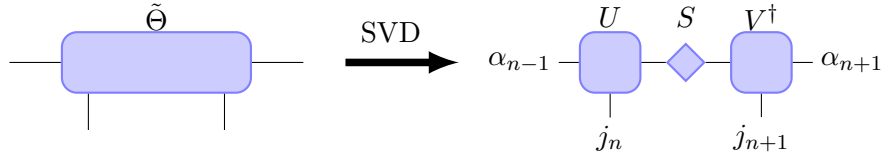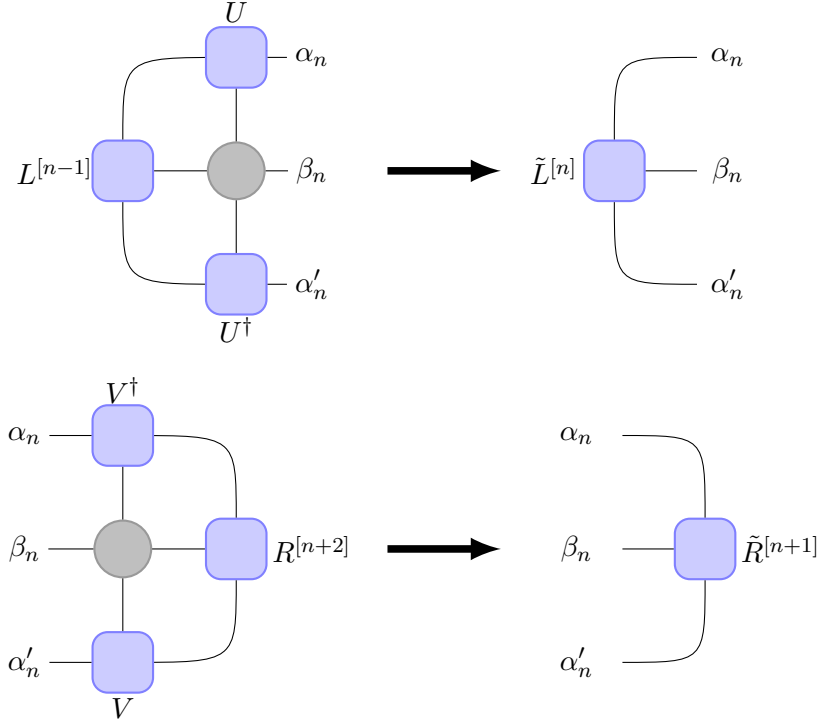
(1) Merge:
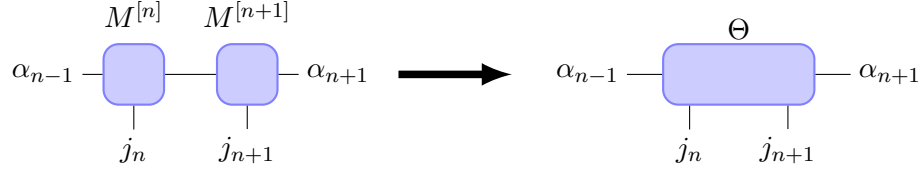
(2) Solve eigenprobem:
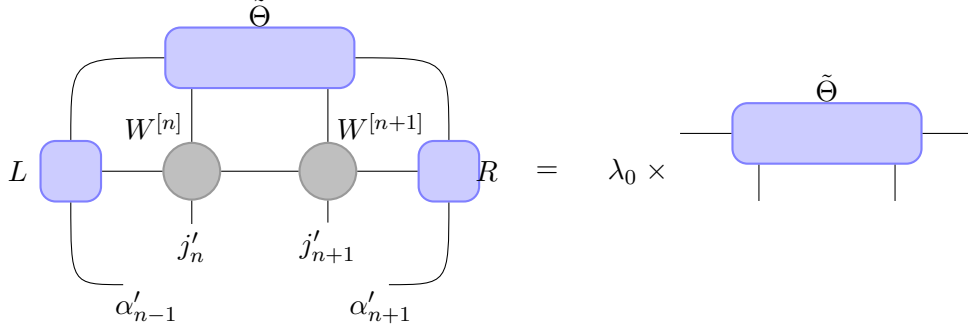
(3) Unmerge:

(4) Update environments:

Figure 21: *A diagrammatic representation of the two-site update sequence for iterative ground state search. In step (4), which environment is updated is determined by the direction of iteration.*

Iterative ground state search algorithm

> **Initialize:** Start from some right-normalized initial guess for $|\psi\rangle$. From this, calculate the tensor $R^{[i]}$ iteratively for all sites, starting at the right.

> **Right sweep:** Starting from site $n = 1$, perform a *two-site update*, where one updates the *left environment* as described in eq. (118). Afterwards, n is iterated by 1, $n \to n+1$, and the process is repeated until $n = N - 1$ is reached.

> **Left sweep:** Starting from site $n = N - 1$, perform a *two-site update*, where one updates the *right environment* as described in eq. (118). Afterwards, n is iterated by 1, $n \to n - 1$, and the process is repeated until $n = 1$ is reached.

> **Repeat sweeps:** Continue by alternating between left and right sweeps through the system until convergence is achieved.

6.3   Calculation of Condensate Fraction using DMRG Algorithm

Recall the Bose-Hubbard Hamiltonian (equation (37)), which supports the two distinct quantum phases: The Superfluid (SF) phase, $U/J \ll 1$, which exhibit long range correlations, and the Mott-Insulator (MI) phase, $U/J \gg 1$, where no interaction between neighboring sites is present. The SF phase is a Bose-Einstein condensate with special attributes, as it exhibits maximal de-localization of the particles and can be approximated as a coherent state. On the other hand, as the individual sites are completely decoupled in the MI phase, no condensate is present.

According to the Penrose-Onsager criterion, a Bose-Einstein condensate, and by extension the SF state, is present if and only if the largest eigenvalue, λ_1, of the single-particle density matrix, $\rho^{(1)}$, is macroscopic

$$f_c = \frac{\lambda_1}{N_{\text{particles}}} > 0 \ , \tag{122}$$

where f_c is the *condensate fraction* and $N_{\text{particles}}$ is the total number of particles [26]. Thus, the condensate fraction can be used to determine which state is the dominant of the system, as

$$\lim_{N_{\text{particles}} \to \infty} f_c^{\text{SF}} \to 1 \tag{123}$$

$$\lim_{N_{\text{particles}} \to \infty} f_c^{\text{MI}} \to 0 \ , \tag{124}$$
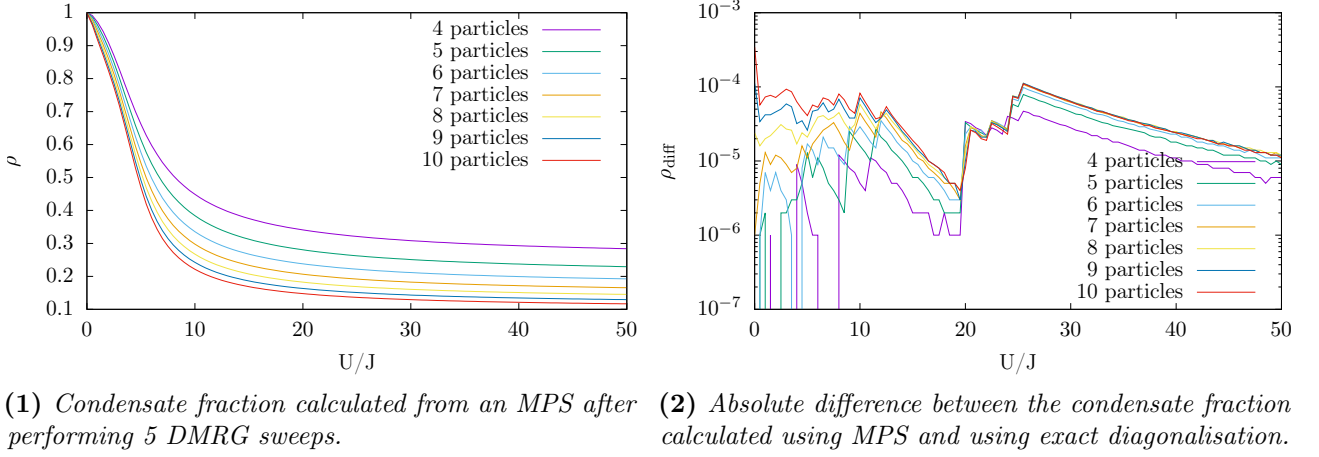
where the filling-fraction $n = N_{\text{particles}}/N_{\text{sites}}$ is held constant. While the limit for the SF phase will be reached for any number of particles, the MI phase will only be reached in the limit $N_{\text{particles}} \to \infty$.
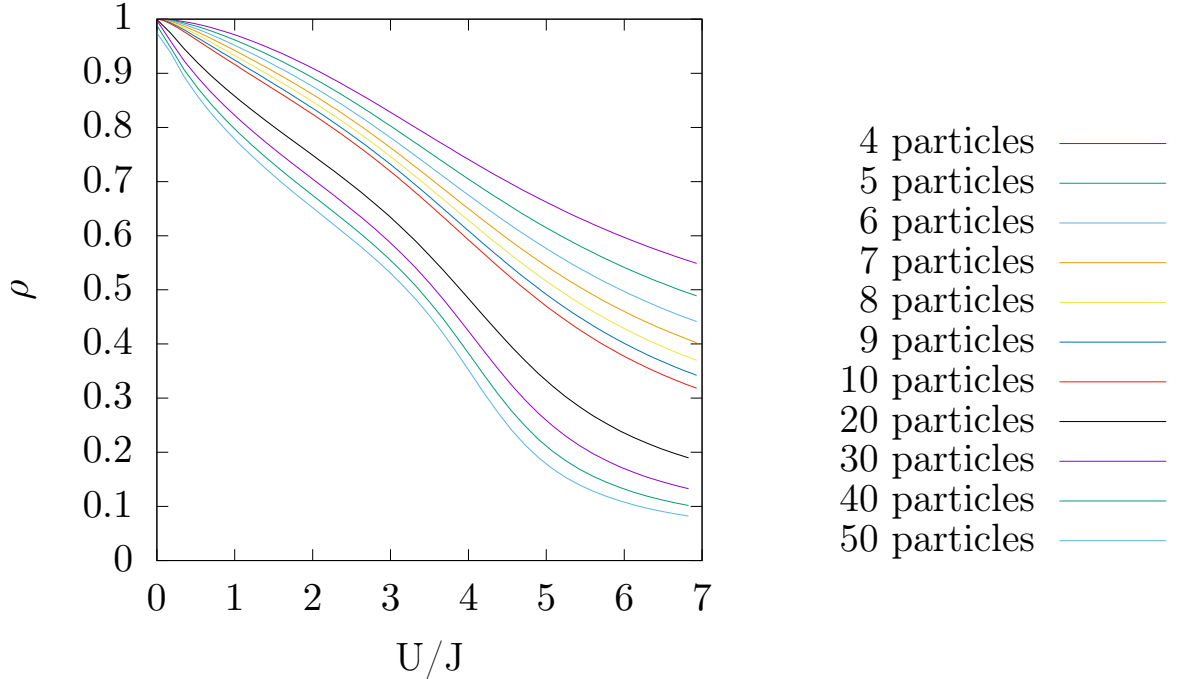
Calculated condensate fractions

In order to test the precision of MPS formalism and the ITensor library, the condensate fraction was calculated for a series of U/J with varying particle number. For this the library's implementation of the DMRG algorithm was used, where the number of sweeps was selected, such that the bond dimension remained the same when adding more sweeps. In this case 5 sweeps with a maximum bond dimension of 200 was sufficient. All calculations were performed with unit occupancy. These results were then compared to a similar calculation using exact diagonalisation.

Figure 221 shows the condensate fraction for various U/J calculated using MPS. In the limit $U/J = 0$ the condensate fraction is unit as expected, thus confirming that the system is indeed in the SF state. The condensate fraction never reaches zero, as this is only achieved in the thermodynamic limit as described by equation (124). However, the condensate fraction does decrease with increasing particle number as would be expected.

In figure 222 the results of the MPS calculation is compared to exact diagonalisation by displaying the absolute difference between the two calculations. It is clear that the two approaches yield very similar results for low particle-number.

(1) *Condensate fraction calculated from an MPS after performing 5 DMRG sweeps.*

(2) *Absolute difference between the condensate fraction calculated using MPS and using exact diagonalisation.*

Attempting to use exact diagonalisation for large particle numbers is futile due to the exponential scaling of the Hilbert space [40], however, as mentioned, this is not an issue using matrix product states, since low contributing eigenstates are truncated. Figure 23 shows the results of the DMRG

Figure 23: *Condensate fraction calculated from an MPS after performing 20 DMRG sweeps.*

calculations for up to 50 particles. The condensate fraction behaves as expected in the $U/J \gg 1$ limit, as it tends towards zero for larger particle numbers. Note, that in the SF limit the condensate fraction does not quite reach 1. However, this can be understood when considering figure 18iv, as the DMRG algorithm is unable to describe the very long ranged correlation of the Superfluid. Smaller systems do not have this issue, as boundary effects has an influence on a much larger part of the system. Thus, these systems barely show any sign of long ranged correlations making them easy to approximate.

Some measures can be taken when using the DMRG algorithm in order to minimize errors. Accurately describing long range correlations requires multiple sweeps, as the algorithm iteratively has to approximate an almost constant function with a series of exponentials. Figure 24 displays the condensate fraction in the Superfluid limit as a function of number of sweeps. Clearly, performing more sweeps yields a better result. Furthermore, one observes numerically, that increasing the maximal bond dimension D results in a more accurate long-range representation of correlations. Thus, calculating correlation functions for various values of D is a great way of estimating the convergence of the correlations for a given length scale [32].

Precision plot for 50 particles
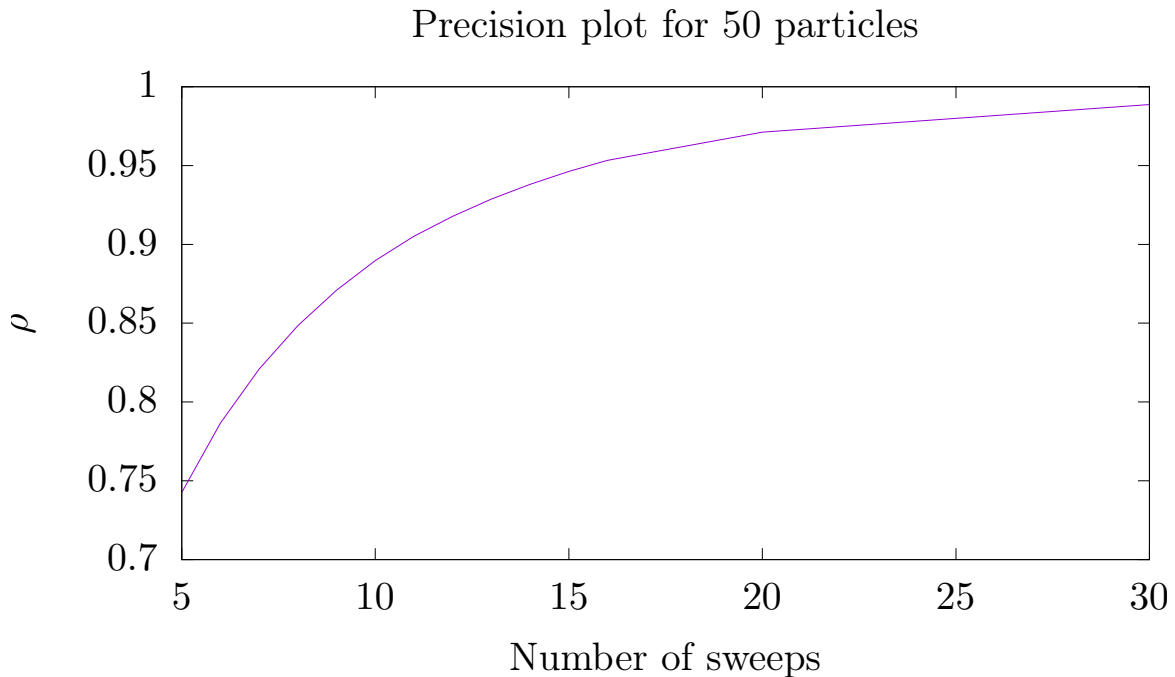
Figure 24: *SF condensate fraction as a function of number of sweeps of the DMRG algorithm. A max bond dimension of 250 was used.*

In [22] the critical point of phase transition between the Superfluid and Mott-Insulator is determined as $\left(\frac{U}{J}\right)_{crit} = 3.37$. This is computed by determining the point at which the Luttinger liquid parameter is $K = \frac{1}{2}$. Examining figure 23 one notices a hump on the graph in the vicinity of this critical ratio, however, no clear indication of a phase transition is present. In the thermodynamic limit one would expect the condensate fraction to drop to zero as the critical ratio is reached (as observed in 2D by [35]), although at 50 particles the condensate fraction is only around 0.5. One could extrapolate data from several computations using different particle numbers in order to determine the location of the critical point. However, this would require computations using larger systems in order to minimize the boundary effects.

7   Performing Time Evolution of Matrix Product States

A central component of Optimal Control is time evolution. In order to compute any optimal control sequence, it is crucial to have a fast and accurate time evolution algorithm. However, also the construction of the time evolution operator must be taken into account, as exponentiating a tensor spanning the entire system, such as most Hamiltonians, is no easy task. In fact, since the time evolution operator is constantly altered when optimizing control parameters, the time spent exponentiating the Hamiltonian must be taken into account of the total runtime. Thus, both an efficient time evolution algorithm and an efficient operator exponentiation is needed when performing optimal control.

Several algorithms for time evolving matrix product states exist, however, they all origin from the same ideas proposed in [40, **?**]. The most widely used of these algorithms is the tDMRG algorithm, which gets its name from its similarity with the ground state search algorithm described in Section 6.2. The tDMRG algorithm has been utilized in several instances to simulate the dynamics of one-dimensional systems CITE, and it has even been previously used in conjunction with the CRAB algorithm to perform optimal control of the Superfluid to Mott-Insulator phase transition CITE.

Although the standard algorithms for time evolution are quite efficient, further improvements can be made to the algorithms when tailoring to the problem at hand. Therefore, a modified version of the tDMRG algorithm is proposed in Section 7.2, which directly utilizes the properties of the Bose-Hubbard Hamiltonian.

7.1   The tDMRG Algorithm

Consider the time evolution of a quantum state

$$|\psi(t)\rangle = \hat{\mathcal{U}}(t)\,|\psi(0)\rangle \ , \tag{125}$$

where $\hat{\mathcal{U}}(t) = \mathrm{e}^{-\mathrm{i}\hat{H}t}$ is the time evolution operator. Time evolution of a matrix product states is done in a manner similar to that of ground state search, as the bonds between the tensors are evolved rather than the tensors themselves. Thus, the time evolution operator must be decomposed into two-site tensors. The simplest realisation of this is achieved, when considering a Hamiltonian containing only nearest-neighbour interactions. Assume the Hamiltonian is a sum of two-site operators of the form $\hat{H} = \sum_n \hat{h}^{[n,n+1]}$. One can decompose this into a sum over even and odd bonds

$$\hat{H} = \hat{H}_{\mathrm{odd}} \ + \ \hat{H}_{\mathrm{even}} = \sum_{n\ \mathrm{odd}} \hat{h}^{[n,n+1]} \ + \ \sum_{n\ \mathrm{even}} \hat{h}^{[n,n+1]} \ . \tag{126}$$

Exponentiating the Hamiltonian is non-trivial due to the non-commutativity of the operators, $[\hat{h}_{\mathrm{odd}}^{[n,n+1]}\,,\ \hat{h}_{\mathrm{even}}^{[n,n+1]}] \neq 0$. Considering a small time slice, δt, the exponentiation can be achieved through the Trotter-Suzuki expansion [36]. To first order this reads

$$\mathrm{e}^{-\mathrm{i}\hat{H}\,\delta t} = \mathrm{e}^{-\mathrm{i}\hat{H}_{\mathrm{odd}}\,\delta t}\,\mathrm{e}^{-\mathrm{i}\hat{H}_{\mathrm{even}}\,\delta t} \ + \ \mathrm{O}(\delta t^2) \ , \tag{127}$$

where the error is due to the non-commutativity of the bond Hamiltonians. Thus, the time evolution operator can be expressed as the product

$$\hat{\mathcal{U}}(\delta t) \approx \left(\prod_{n\ \mathrm{odd}} \hat{\mathcal{U}}^{[n,n+1]}(\delta t)\right)\left(\prod_{n\ \mathrm{even}} \hat{\mathcal{U}}^{[n,n+1]}(\delta t)\right) \ , \tag{128}$$

where

$$\hat{\mathcal{U}}^{[n,n+1]}(\delta t) = \mathrm{e}^{-\mathrm{i}\hat{h}^{[n,n+1]}\,\delta t} \ . \tag{129}$$

The result is an MPO performing an infinitesimal time step on the odd bonds, and another MPO evolving the even bonds. An illustration of this is shown in Figure 25. The tDMRG algorithm describes
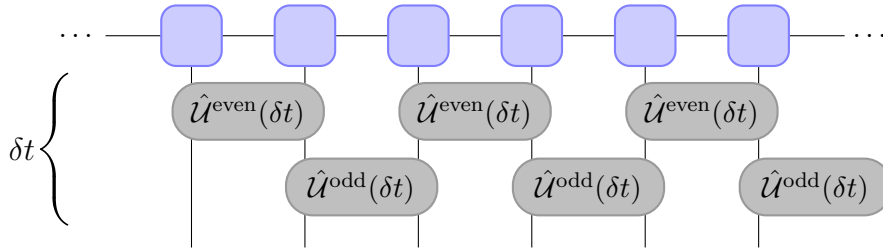
Figure 25: *Approximation of each time step δt using a Trotter-Suzuki decomposition, such that the time evolution operator is expressed as a product of unitary two-site operators.*

the most efficient and accurate way of contracting the tensor network detailed in Figure 25. The algorithm gets its name from its similarity with the DMRG algorithm detailed in Section 6.2. In fact, the merge and unmerge procedure of the two algorithms is completely identical, whereby they only differ in the steps of applying the operator and proceeding to the next site. The following procedure details a time evolution step of the n'th bond [**?**].

Infinitesimal time-step update for tDMRG

1. **Merge:** Contract tensors $M^{[n]}$ and $M^{[n+1]}$ over the bond α_n creating a two-site tensor $\Theta^{j_n,j_{n+1}}$.

2. **Apply unitary:** The two-site time evolution operator, $\hat{\mathcal{U}}^{[n,n+1]}$, is applied to $\Theta^{j_n,j_{n+1}}$

$$\tilde{\Theta}^{j_n,j_{n+1}}_{\alpha_{n-1},\alpha_{n+1}} = \sum_{j'_n,j'_{n+1}} U^{j_n j_{n+1},j'_n j'_{n+1}}\ \Phi^{j'_n,j'_{n+1}}_{\alpha_{n-1},\alpha_{n+1}} \ . \tag{130}$$

3. **Unmerge:** Reshape $\tilde{\Phi}^{j'_n, j'_{n+1}}_{\alpha_{n-1}, \alpha_{n+1}}$ to a matrix and decompose it through an SVD. Applying $\hat{\mathcal{U}}^{[n,n+1]}$ causes an increase in bond dimension, $D \to d^2 D$, which must be truncated by keeping only the D largest singular values from the SVD.

4. **Progress:** Next, the center cite of the MPS must be shifted by two, in order to update the next even (odd) bond. This is achieved by merging tensors $M^{[n+1]}$ and $M^{[n+2]}$ and performing a second SVD, while reshaping the resulting U-matrices to left-normalised tensors to retain the canonical form. The product of the second SVD must be truncated as well, however, no loss of information will occur, as the Schmidt rank of the matrix S will be at most D following the first SVD.

Following the procedure will leave the MPS in position for application ofthe unitary $\hat{\mathcal{U}}^{[n+2,n+3]}$. The efficiency of the tDMRG algorithm also depends on the sequence in which bonds are evolved. A simple, yet effective way is iterating from left to right when evolving even bonds, while iterating right to left when evolving odd bonds. Thereby, the centered cite of the mixed-canonical form is moved continuously through the MPS, rather than having to be reset when reaching the end of the system.

Although the tDMRG algorithm is a very powerful algorithm, an even higher efficiency can be achieved when tailoring the algorithm to the problem. In this case the problem is optimal control of the Superfluid to Mott-Insulator transition. Thus, the Hamiltonian contains both nearest-neighbour and on-site terms. Furthermore, the Hamiltonian is time dependent, and it is continuously modified in the process of searching for optimal control parameters. The following algorithm is a modification of the tDMRG algorithm, which accommodates the requirements of performing optimal control.

7.2 Modified Time Evolution Algorithm for Optimal Control

In order to efficiently conduct optimal control of a Bose-Hubbard system, a slightly modified version of the tDMRG algorithm was employed. As the Hamiltonian is changing with every time step, one has to account for the time spent exponentiating the operators when considering the runtime of the algorithm. A general operator $\hat{W}$ can be exponentiated through the series expansion

$$\exp\left(\hat{W}\right) = \sum_{k=0}^{\infty} \frac{\hat{W}^k}{k!} = \hat{\mathbb{1}} + \hat{W}\left(\hat{\mathbb{1}} + \frac{\hat{W}}{2}\left(\hat{\mathbb{1}} + \frac{\hat{W}}{3}\left(\dots \right.\right.\right. \tag{131}$$

The number of terms needed in the expansion to accurately describe the exponentiation depends on the operator. Performing the exponentiation through a series expansion is a relatively expensive operator. Therefore, it is crucial to find an easier way of constructing the time evolution operator. One method is by considering the form of the Bose-Hubbard Hamiltonian. The most natural choice of control parameter is the lattice depth, V_0, as it is controllable experimentally. The lattice depth determines both the tunneling matrix element, J (eq. (36)), and the interaction matrix element, U (eq. (38)), and has served as control parameter in other studies CITE. Unfortunately exponentiating the hopping terms of the Bose-Hubbard Hamiltonian was relatively high. Therefore, it was concluded that keeping J fixed and using U as the control parameter was the better option. Due to the diagonal form of the number operator, $\hat{n}_i$, the exponentiation of the interaction term can be built directly without the need for the series expansion of eq. (131). However, simply exponentiating the different terms of the Bose-Hubbard Hamiltonian separately is not possible, as the operators do not commute. Therefore, one must expand the time evolution operator into its components through the Suzuki-Trotter expansion. To second order the Suzuki-Trotter expansion reads
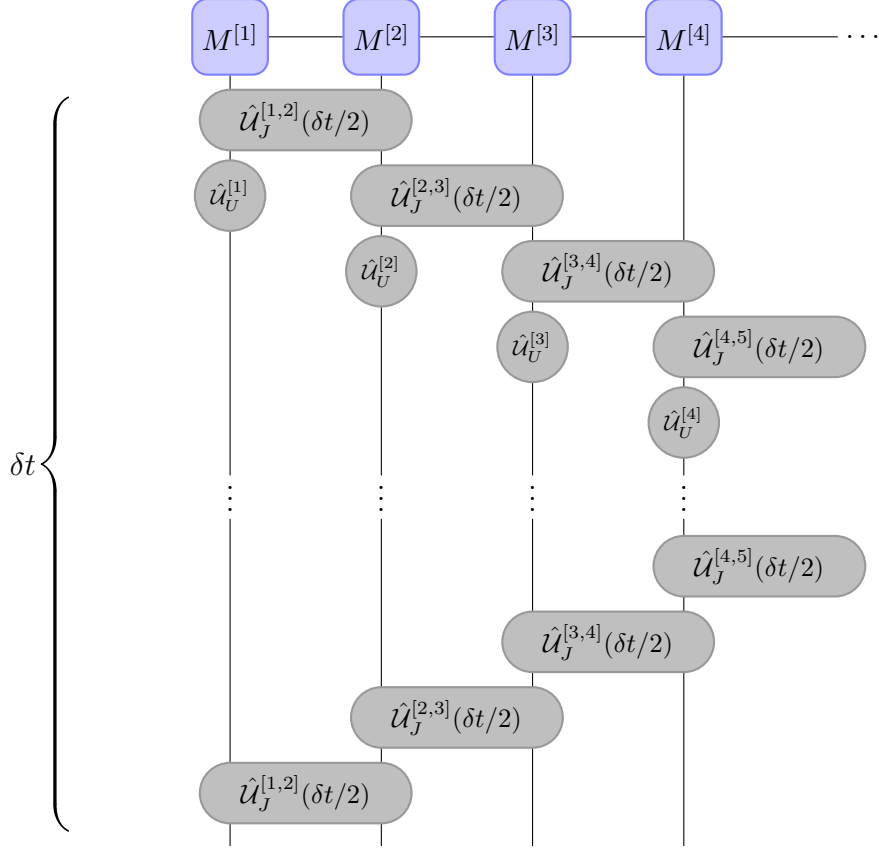
$$\exp\left((\hat{V} + \hat{W})\delta\right) = \exp\left(\hat{V}\delta/2\right)\exp\left(\hat{W}\delta\right)\exp\left(\hat{V}\delta/2\right) + O(\delta^3) \,. \tag{132}$$

Once again, the error is due to the non-commutativity of operators. Thus, the time evolution operator can be divided into a sequence of tensors, where

$$\hat{\mathcal{U}}_J^{[i,i+1]}(\delta t/2) = \exp\left(-iJ(\hat{a}_i^\dagger \hat{a}_{i+1} + \hat{a}_{i+1}^\dagger \hat{a}_i)\frac{\delta t}{2}/\hbar\right) \tag{133}$$

$$\hat{\mathcal{U}}_U^{[i]}(\delta t) = \exp\left(-i\frac{U}{2}\hat{n}_i(\hat{n}_i - 1)\delta t/\hbar\right) . \tag{134}$$

A single time step, δt, using the expanded operator is represented diagrammatically in figure 26. At

Figure 26: *Tensor diagram depicting a single time step of the modified rDMRG algorithm. The time evolution operator has been subjected to a Suzuki-Trotter expansion as detailed in eq. (132). The tensors of the upper part of the network are contracted with the MPS while sweeping from left to right, whereas the lower part is applied with a right to left sweep.*

first glance, the tensor network resulting from the Suzuki-Trotter expansion may seem rather extensive, however, it can be contracted in a very efficient manner. The upper part of the network is contracted in a left to right sweeping manner, where the position of the center cite, and thereby the normalisation of the MPS, is pushed to the right following each step. The sequence of contractions is shown in figure 27. The MPS is initially centered on the first tensor, while its remaining tensors are all right-normalised. By contracting the bonds marked with a bold line, the operators are efficiently applied to the MPS. In step (iii) the two-site tensor, Θ, is split using an SVD, where the bond dimension of the tensors is truncated. This is crucial in order to maintain a reduced dimensionality, which would otherwise result in a significant increase in contraction time. In the last step the MPS is centered on the next site, leaving the previous center left-normalised. Thereby the normalisation of the MPS is "pushed" to the right and contained in a single site, which makes it easy to deal with in the end of the time evolution step. As the center reaches the end of the MPS, the direction of the sweep is reversed. The right to left sweep is slightly different, as there are no $\hat{\mathcal{U}}_U$-tensors that need to be contracted. The time evolution step is completed, as the first site is reached.

Comparing the original tDMRG with the modified version reveals a difference in the ordering of the two-site operators. The tDMRG algorithm evolves all even bonds first followed by an evolution
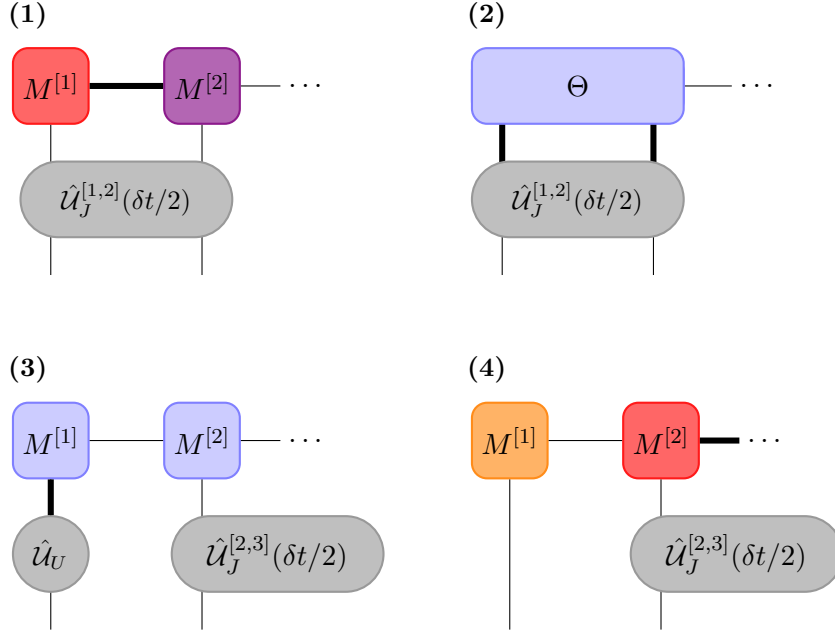
Figure 27: *Sequence of contractions for modified tDMRG algorithm during left to right sweep. Step (i): MPS centred on site 1, tensors $A^{[1]}$ and $A^{[2]}$ are contracted. Step (ii): Two-site tensor is contracted with two-site operator, followed by a splitting of the resulting tensor through an SVD in step (iii). Lastly, in step (iv), the center (and thereby the normalisation) is pushed to the next site leaving $A^{[1]}$ left-normalised.*

of the odd bonds. Meanwhile, the modified algorithm applies the two-site operators in a sweeping manner, as the central site of the MPS is moved. The most accurate approach is the original tDMRG algorithm. However, following the structure of the modified algorithm, evolving even and odd bonds separately would require multiple sweeps back and forth, due to the second order of the Suzuki-Trotter decomposition. The result is a large increase in the number of SVD's needed, which is a fairly expensive operation to perform. Therefore, the modified algorithm employs the less accurate order of operations. Since the Suzuki-Trotter expansion is of second order, compared to the first order used in the regular tDMRG algorithm, the error may be compensated. To properly gauge the accuracy of this time evolution operator, it must be compared to the more reliable approach of direct diagonalisation.

## 7.3 Numerical Comparison of Time Evolution Algorithms

A Diagrammatic Representation of Matrix Product States

An MPS and any operations on it can be descibed graphically using tensor networks, which allows for a visual overview of the mathematics taking place. For instance, one can represent a single tensor in the MPS as seen in figure 281, where horizontal legs are called *bond dimensons* and represent the indiced of the local matrix. The vertical legs correspond to the physical index of the site. These tensors can be contracted by connecting the legs of tensors as seen in figure 282. Connected lines are summed over just like matrix multiplication.
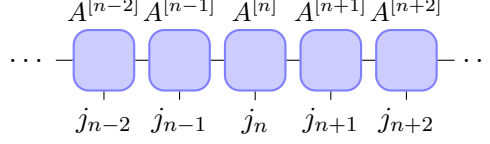
B Example: Building an MPO from a Hamiltonian

Consider the Bose-Hubbard Hamiltonian , which consists of both nearest-neighbour tunneling terms and on-site interactions terms

$$\hat{H} = -J \sum_{\langle i,j \rangle} \hat{a}_i^\dagger \hat{a}_j + \frac{U}{2} \sum_i \hat{n}_i \left(\hat{n}_i - 1 \right) \ . \tag{135}$$
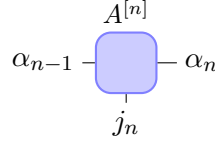
(1) *Single tensor of an MPS. The horizontal legs are the indices of the local matrix, while the vertical leg is physical index of the site.*

(2) *Simple connected network of tensors. Connected lines are summed over.*

The Hamiltonian can be expressed as a sum of strings of operators - most of these being identities just like in equation 90. Moving through such a string from the right, one will at some point encounter one of 3 non-trivial operators. This can be summarized as 4 different possible states of the string of operators on a given bond:

1. Only identities to the right of the bond.

2. An $\hat{a}^\dagger$ operator just to the right of the bond.

3. An $\hat{a}$ operator just to the right of the bond.

4. A completed tunneling *or* the interaction term, $\frac{U}{2}\hat{n}(\hat{n}-1)$, somewhere to the right.

When moving through the string of operators from the right, only certain transitions between these state are possible. For instance $\mathbf{1 \to 1}$, where one starts in state 1, and the next operator is an identity. Likewise, $\mathbf{1 \to 2, 3, 4}$ are all possible, since these transitions represent the next operator being non-trivial. Next, $\mathbf{2 \to 4}$ completes the hopping $-J\hat{a}^\dagger\hat{a}$ - a similar transition exists for the other hopping term $\mathbf{3 \to 4}$. Finally, the transition $\mathbf{4 \to 4}$ is needed to continue iterating through the operator chain after having passed the non-trivial operators. This can be encoded in the operator-valued matrix

$$W^{[i]} = \begin{pmatrix} \hat{I} & 0 & 0 & 0 \\ \hat{a}^\dagger & 0 & 0 & 0 \\ \hat{a} & 0 & 0 & 0 \\ \frac{U}{2}\hat{n}(\hat{n}-1) & -J\hat{a} & -J\hat{a}^\dagger & \hat{I} \end{pmatrix}, \tag{136}$$

which contains all the allowed transitions between the five state [**?**]. When one starts moving through the operator chain from the right side, one obviously begins in state 1 and ends in state 4. This can be encoded in the two vectors

$$\vec{v}_{left} = (0, 0, 0, 1) \quad, \quad \vec{v}_{right} = (1, 0, 0, 0)^T .$$

Thus, the Bose-Hubbard Hamiltonian can be written as an MPO

$$\hat{H} = \sum_{\boldsymbol{j},\boldsymbol{j'}} \vec{v}_{left} \, W^{[1]j_1,j_1'} W^{[2]j_2,j_2'} \dots W^{[N]j_N,j_N'} \, \vec{v}_{right} \, |\boldsymbol{j}\rangle \langle \boldsymbol{j'}| . \tag{137}$$

Often, the two closing vectors are implicitly multiplied unto the outer matrices for a cleaner notation. Observe how all of this was done without having to do a single numerical computation. The resulting MPO can now readily be applied to an MPS.

Bibliography

[1] Mike H Anderson, Jason R Ensher, Michael R Matthews, Carl E Wieman, Eric A Cornell, et al. Observation of bose-einstein condensation in a dilute atomic vapor. *science*, 269(5221):198–201, 1995.

[2] Immanuel Bloch, Jean Dalibard, and Sylvain Nascimbene. Quantum simulations with ultracold quantum gases. *Nature Physics*, 8(4):267–276, 2012.

[3] Immanuel Bloch, Jean Dalibard, and Wilhelm Zwerger. Many-body physics with ultracold gases. *Rev. Mod. Phys.*, 80:885–964, Jul 2008.

[4] H. Bruus and K. Flensberg. *Many-Body Quantum Theory in Condensed Matter Physics: An Introduction*. Oxford Graduate Texts. OUP Oxford, 2004.

[5] Claude Cohen-Tannoudji, Jacques Dupont-Roc, Gilbert Grynberg, and Patricia Thickstun. *Atom-photon interactions: basic processes and applications*. Wiley Online Library, 1992.

[6] Jean Dalibard, Fabrice Gerbier, Gediminas Juzeliūnas, and Patrik Öhberg. Colloquium: Artificial gauge potentials for neutral atoms. *Reviews of Modern Physics*, 83(4):1523, 2011.

[7] J. Eisert, M. Cramer, and M. B. Plenio. Colloquium: Area laws for the entanglement entropy. *Rev. Mod. Phys.*, 82:277–306, Feb 2010.

[8] Satoshi Ejima, Holger Fehske, Florian Gebhard, Kevin zu Münster, Michael Knap, Enrico Arrigoni, and Wolfgang von der Linden. Characterization of mott-insulating and superfluid phases in the one-dimensional bose-hubbard model. *Phys. Rev. A*, 85:053644, May 2012.

[9] Nathan Gemelke, Xibo Zhang, Chen-Lung Hung, and Cheng Chin. In situ observation of incompressible mott-insulating domains in ultracold atomic gases. *Nature*, 460(7258):995, 2009.

[10] Markus Greiner. *Ultracold quantum gases in three-dimensional optical lattice potentials*. PhD thesis, April 2003.

[11] Rudolf Grimm, Matthias Weidemüller, and Yurii B. Ovchinnikov. Optical dipole traps for neutral atoms. volume 42 of *Advances In Atomic, Molecular, and Optical Physics*, pages 95 – 170. Academic Press, 2000.

[12] E. P. Gross. Structure of a quantized vortex in boson systems. *Il Nuovo Cimento (1955-1965)*, 20(3):454–477, May 1961.

[13] M. B. Hastings. An area law for one-dimensional quantum systems. *Journal of Statistical Mechanics: Theory and Experiment*, 2007(08):P08024, 2007.

[14] D. Jaksch, H.-J. Briegel, J. I. Cirac, C. W. Gardiner, and P. Zoller. Entanglement of atoms via cold controlled collisions. *Phys. Rev. Lett.*, 82:1975–1978, Mar 1999.

[15] D. Jaksch, C. Bruder, J. I. Cirac, C. W. Gardiner, and P. Zoller. Cold bosonic atoms in optical lattices. *Phys. Rev. Lett.*, 81:3108–3111, Oct 1998.

[16] D. Jaksch and P. Zoller. The cold atom hubbard toolbox. *Annals of Physics*, 315(1):52 – 79, 2005. Special Issue.

[17] V. A. Kashurnikov, N. V. Prokof'ev, and B. V. Svistunov. Revealing the superfluid˘mott-insulator transition in an optical lattice. *Phys. Rev. A*, 66:031601, Sep 2002.

[18] C. Kittel. *Introduction to Solid State Physics*. Wiley, 2004.

[19] Charles Kittel and Ching-yao Fong. *Quantum theory of solids*, volume 3. Wiley New York, 1963.

[20] Walter Kohn. Analytic properties of bloch waves and wannier functions. *Physical Review*, 115(4):809, 1959.

[21] C. Kollath, U. Schollwöck, J. von Delft, and W. Zwerger. Spatial correlations of trapped one-dimensional bosons in an optical lattice. *Phys. Rev. A*, 69:031601, Mar 2004.

[22] Till D. Kühner, Steven R. White, and H. Monien. One-dimensional bose-hubbard model with nearest-neighbor interaction. *Phys. Rev. B*, 61:12474–12489, May 2000.

[23] Cornelius Lanczos. An iteration method for the solution of the eigenvalue problem of linear differential and integral operators. *J. Res. Natl. Bur. Stand. B*, 45:255–282, 1950.

[24] Maciej Lewenstein, Anna Sanpera, Veronica Ahufinger, Bogdan Damski, Aditi Sen(De), and Ujjwal Sen. Ultracold atomic gases in optical lattices: mimicking condensed matter physics and beyond. *Advances in Physics*, 56(2):243–379, 2007.

[25] Ian P McCulloch. From density-matrix renormalization group to matrix product states. *Journal of Statistical Mechanics: Theory and Experiment*, 2007(10):P10014, 2007.

[26] Oliver Penrose and Lars Onsager. Bose-einstein condensation and liquid helium. *Phys. Rev.*, 104:576–584, Nov 1956.

[27] Christopher J Pethick and Henrik Smith. *Bose-Einstein condensation in dilute gases*. Cambridge university press, 2002.

[28] L.P. Pitaevskii. Vortex lines in an imperfect bose gas. *Soviet Physics JETP*, 13(2):451–454, August 1961.

[29] M. Plischke and B. Bergersen. *Equilibrium Statistical Physics*. World Scientific, 2006.

[30] Subir Sachdev. *Quantum phase transitions*. Wiley Online Library, 2007.

[31] M. Saffman, T. G. Walker, and K. Mølmer. Quantum information with rydberg atoms. *Rev. Mod. Phys.*, 82:2313–2363, Aug 2010.

[32] Ulrich Schollwöck. The density-matrix renormalization group in the age of matrix product states. *Annals of Physics*, 326(1):96 – 192, 2011. January 2011 Special Issue.

[33] Norbert Schuch, Michael M. Wolf, Frank Verstraete, and J. Ignacio Cirac. Entropy scaling and simulability by matrix product states. *Phys. Rev. Lett.*, 100:030504, Jan 2008.

[34] Jonathan Simon, Waseem S Bakr, Ruichao Ma, M Eric Tai, Philipp M Preiss, and Markus Greiner. Quantum simulation of antiferromagnetic spin chains in an optical lattice. *Nature*, 472(7343):307–312, 2011.

[35] I. B. Spielman, W. D. Phillips, and J. V. Porto. Condensate fraction in a 2d bose gas measured across the mott-insulator transition. *Phys. Rev. Lett.*, 100:120402, Mar 2008.

[36] Masuo Suzuki. General theory of fractal path integrals with applications to many-body theories and statistical physics. *Journal of Mathematical Physics*, 1991.

[37] Leticia Tarruell, Daniel Greif, Thomas Uehlinger, Gregor Jotzu, and Tilman Esslinger. Creating, moving and merging dirac points with a fermi gas in a tunable honeycomb lattice. *Nature*, 483(7389):302–305, 2012.

[38] D. van Oosten, P. van der Straten, and H. T. C. Stoof. Quantum phases in an optical lattice. *Phys. Rev. A*, 63:053601, Apr 2001.

[39] G. Vidal. Classical simulation of infinite-size quantum lattice systems in one spatial dimension. *Phys. Rev. Lett.*, 98:070201, Feb 2007.

[40] Guifré Vidal. Efficient classical simulation of slightly entangled quantum computations. *Phys. Rev. Lett.*, 91:147902, Oct 2003.

[41] Steven R. White. Density matrix formulation for quantum renormalization groups. *Phys. Rev. Lett.*, 69:2863–2866, Nov 1992.

[42] Steven R. White. Density matrix renormalization group algorithms with a single center site. *Phys. Rev. B*, 72:180403, Nov 2005.

[43] Artur Widera. *Constructing correlated spin states with neutral atoms in optical lattices*. PhD thesis, Ph. D. thesis, Johannes Gutenberg-Universität, Mainz, 2008.